CrossMark

Reconstruction of Galaxy Star Formation Histories through SED Fitting: The Dense Basis Approach

Kartheik Iyer and Eric Gawiser
Department of Physics and Astronomy Rutgers, The State University of New Jersey, 136 Frelinghuysen Road,
Piscataway, NJ 08854-8019, USA; kgi1@physics.rutgers.edu

Abstract

We introduce the dense basis method for Spectral Energy Distribution (SED) fitting. It accurately recovers traditional SED parameters, including M_*, SFR, and dust attenuation, and reveals previously inaccessible information about the number and duration of star formation episodes and the timing of stellar mass assembly, as well as uncertainties in these quantities. This is done using basis star formation histories (SFHs) chosen by comparing the goodness-of-fit of mock galaxy SEDs to the goodness-of-reconstruction of their SFHs. We train and validate the method using a sample of realistic SFHs at $z = 1$ drawn from stochastic realizations, semi-analytic models, and a cosmological hydrodynamical galaxy formation simulation. The method is then applied to a sample of 1100 CANDELS GOODS-S galaxies at $1 < z < 1.5$ to illustrate its capabilities at moderate S/N with 15 photometric bands. Of the six parametrizations of SFHs considered, we adopt linear-exponential, bessel-exponential, log-normal, and Gaussian SFHs, and reject the traditional parametrizations of constant (Top-Hat) and exponential SFHs. We quantify the bias and scatter of each parametrization. 15% of galaxies in our CANDELS sample exhibit multiple episodes of star formation, with this fraction decreasing above $M_* > 10^{9.5}\,M_\odot$. About 40% of the CANDELS galaxies have SFHs whose maximum occurs at or near the epoch of observation. The dense basis method is scalable and offers a general approach to a broad class of data-science problems.

Key words: galaxies: evolution – galaxies: star formation – techniques: photometric

1. Introduction

The integrated light of a galaxy offers a vast amount of information. When measured with sufficient precision and suitably analyzed, the spectral energy distribution (SED) offers insights about a galaxy's composition from its birth to its time of observation (Conroy & Gunn 2010; Acquaviva et al. 2011). This can be used to estimate the galaxy's star formation rate as a function of time, which traces its evolution and merger history (Heavens et al. 2000; Tojeiro et al. 2007; Chevallard & Charlot 2016; Leja et al. 2016). Combined with other observations, this provides valuable knowledge of cosmic structure formation.

Existing methods of SED fitting use a variety of sophisticated techniques. These include inversion methods (Heavens et al. 2000), bayesian codes for estimating uncertainties and covariances (Acquaviva et al. 2015; Chevallard & Charlot 2016), machine learning methods with training sets (Leistedt & Hogg 2016), and template-based models (Bolzonella et al. 2000). To search the large parameter spaces of the variables in consideration, Markov Chain Monte Carlo methods have become increasingly popular.

These advances have been necessitated by the increasing detail provided by theory and the expanding size of galaxy catalogs available through surveys. A large amount of (spectro) photometric data of unprecedented quality will be generated in upcoming surveys, like LSST (Ivezic et al. 2008), HETDEX (Papovich et al. 2016), and J-PAS (Benitez et al. 2014). SDSS (Eisenstein et al. 2011) has already measured spectrophotometry for $\sim 10^6$ objects. The HETDEX/SHELA field will cover roughly 600,000 objects with multi-band photometry and fiber spectroscopy. J-PAS will cover 9000 square degrees with 59 filters (*ugriz*+54 narrow-band filters across optical) for $\sim 9 \times 10^7$ galaxies. Large regions covered in the NIR with Euclid (Laureijs et al. 2010) and WFIRST (Green et al. 2012) will overlap with LSST, which leads to SEDs for $\sim 10^8$ objects by 2022, many of which will have panchromatic photometry. In keeping with the large amounts of reduced data generated by these collaborations, it is imperative that advanced methods of analysis are developed in order to gain useful information from the integrated light of the galaxies under consideration.

The star formation history (SFH) of a galaxy can sometimes be poorly constrained through different approaches to SED fitting. Typical methods assume a predetermined parametrization, like constant star formation or exponentially declining star formation to estimate physical quantities of interest like the stellar mass, star formation rate (SFR), or the time at which the galaxy started forming stars. A few approaches instead seek to reconstruct the SFH from the data, using methods that include reducing the dimensionality of the parameter space using data compression methods (Heavens et al. 2000), fine-binning the interval that makes the maximum contribution to flux (Tojeiro et al. 2007), mapping the discretized-time photometric fitting to a linear inversion problem (Dye 2008), or comparing against a large basis of realistic model SEDs using a Bayesian method (Pacifici et al. 2012). In the current work, we aim to show that using a well-motivated basis allows us to reconstruct robust SFHs from galaxy SEDs.

The paper is organized as follows. In Section 2, we introduce the Dense Basis formalism of SED Fitting, and how it can be applied to the specific problem of reconstructing SFHs, including the motivation for a particular choice of basis and the fitting procedure with a particular basis set. We describe the training of the atlas using different sources of realistic SFHs: SAMs and hydrodynamic simulations, and stochastic SFHs in Section 3. In Section 4, we validate the method on both synthetic SEDs from the SAMs as well as real SEDs from the CANDELS GOODS-S field. We then present results in Section 5 including the number of episodes of star formation
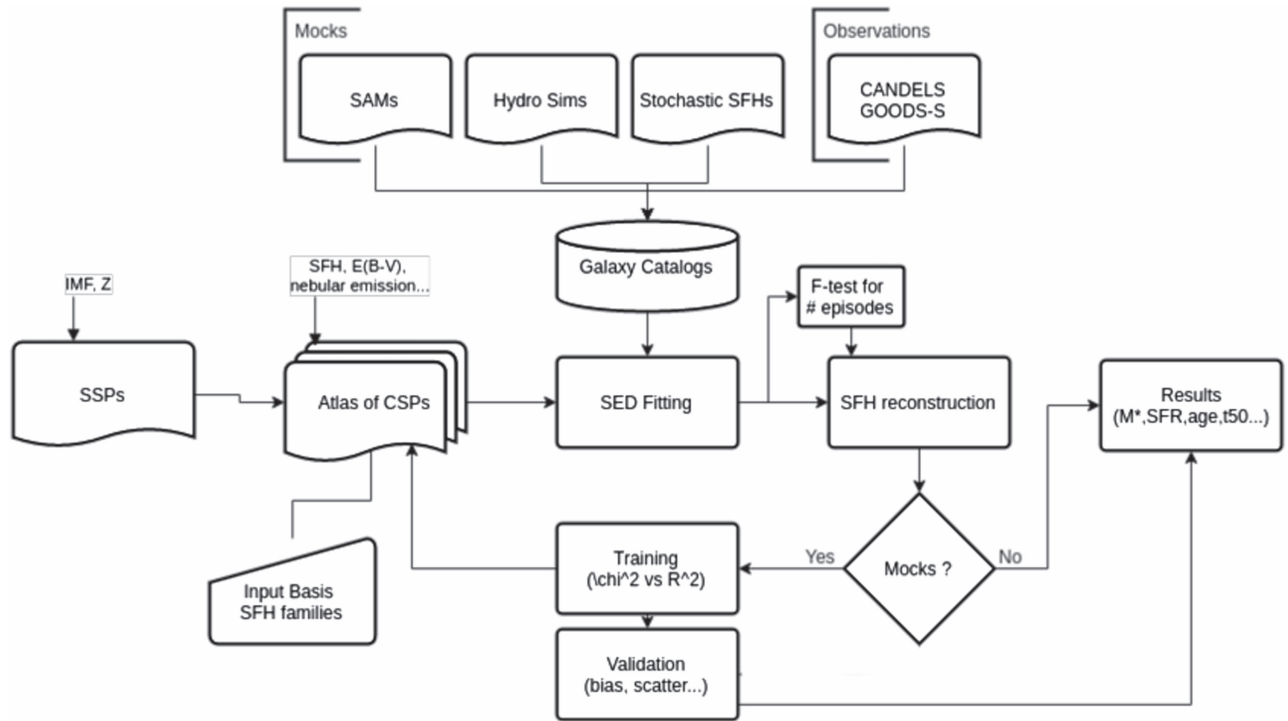
Figure 1. Schematic workflow describing the current implementation of the dense basis method to the reconstruction of star formation histories through photometric SED fitting.

in the galaxy's past and constraints on the timing and duration of star formation activity, quantities that were previously inaccessible through SED fitting. In Section 6, we discuss biases introduced by adopting single parametrizations of SFHs, compare with other SFH reconstruction methods, and mention the application of the dense basis method to larger data sets.

2. The Dense Basis Formalism

The Dense Basis SED fitting method reconstructs SFHs of individual galaxies using an atlas comprised of SEDs corresponding to well-motivated families of SFHs that effectively cover the space of all physical SFHs.[1] It does so by training the atlas on mock catalogs prior to fitting the full data set. This allows us to use the reconstructed SFHs to perform novel analyses and to tackle problems that were previously intractable with SED fitting, such as estimating the number and duration of star formation episodes in a galaxy's past. To avoid any bias due to choice of prior, the method is currently implemented in a frequentist manner. In this section, we briefly describe the dense basis methodology and training of the basis set. An overview of the process is described in Figure 1.

2.1. A Well-motivated Basis of SFHs

The collection of multiple families of well-motivated SFHs and their corresponding SEDs with which we fit galaxies; henceforth, the atlas of SEDs and SFHs should be designed to utilize the dense basis method to its full potential. The choice of

appropriate families of functions to best describe the formation of stars in the galaxy in SFH space (SFR versus t) determines how the SED-fitting procedure encodes realistic star formation. We employ seven major considerations in the choice of the basis that should be satisfied for every functional family under consideration.

1. *Physically or empirically motivated:* The functional form of the SFH needs to be realistic, arising either from statistical analysis of star formation in model galaxies, or deduced from observed galaxies. For the latter, as in Gladders et al. (2013), skewed distributions such as linear rise followed by exponential decline and log-normal rise in physical processes restricted to non-negative domains. In this case, SFHs should also satisfy $SFR|_{t=0} \sim 0$ at the big bang.

2. *Robustness of reconstruction:* The family of basis SFHs should be chosen such that a good fit in an SED space ($[F_\nu, \lambda]$) should correspond to a good reconstruction in SFH space ($[SFH(t), t]$). This correspondence can be tested in various ways and could potentially be different for different data sets since the representative form of the SFH could differ across epochs. It is a useful metric for eliminating SFH families that fit SEDs well but yield biased SFH results, such as exponentially declining SFH parametrizations, which describe star formation reasonably well at recent times, but bias quantities such as age and t_{50}, the lookback time at which the galaxy accumulates 50% of its observed mass, (Pacifici et al. 2012). Analogous to isochrone synthesis and matrix inversion methods, this is possible since the SEDs are piecewise linear in their dependence on the SFH and can be decomposed into multiple representations using different functional families.

3. *Dense in SFH space:* To avoid degeneracies and biases (i.e., to better reveal the local minima of the

---

[1] While an expansion using an infinite number of polynomials or a fourier decomposition would provide a true basis in the sense of spanning the space of all possible curves, our basis functions only do so approximately; however, since they can reconstruct any SFH to the level of precision attainable with spectrophotometric data, they provide an effective basis.
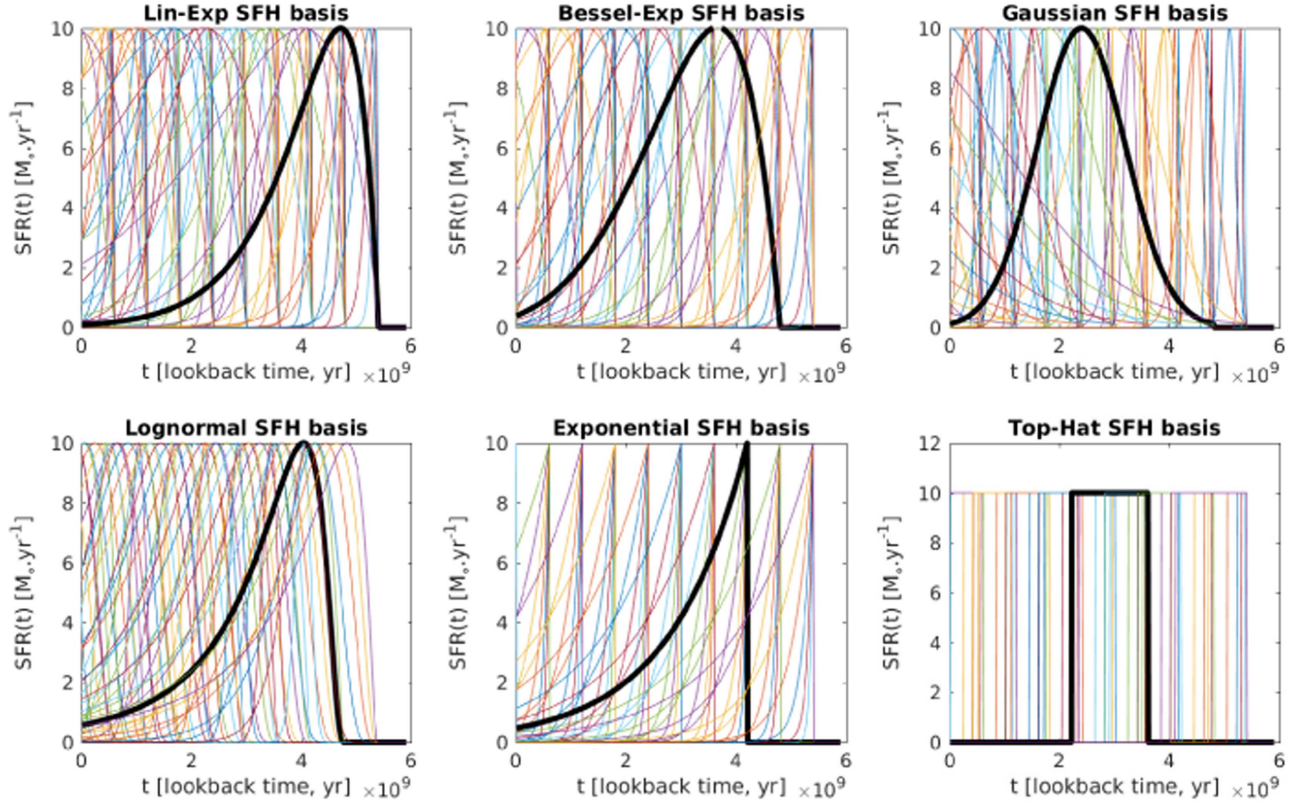
Figure 2. Representative examples of the SFHs at $z = 1$ for the different functional families described in Section 2.2. The full atlas for the dense basis method is constructed using all physical combinations of the Linexp, Besselexp, Gaussian, and log-normal families. A representative curve is shown in bold for each family.

likelihood surface in parameter space), we need to ensure that the basis is sufficiently dense in the space of n-parameter curves spanning SFR(t) in the interval $t \in [0, t_{obs}]$.

4. *Minimal number of parameters:* The number of parameters used to describe the functional form of the SFH basis functions will determine the amount of data compression possible in reconstructing the spectrum of the galaxy from its best-fit coordinates in parameter space: SED(M_*, SFR(t), $Z(t)$, A_v, ...). For the present application, we model the SFH as a sum of star formation basis functions, each needing three parameters to describe each reconstructed episode of star formation, the timing of the peak, the timescale, and the stellar mass formed.

5. *Temporally consistent:* The families should be chosen such that they produce consistent results for an SFH, independent of when the galaxy is observed, within uncertainties.

6. *Positive definite:* Any functional used to describe the SFH should be positive definite, since SFR(t) $\geqslant 0$, $t \in [0, t_{obs}]$, which allows us to extract physical information from multicomponent solutions to the reconstructed SFH, as opposed to methods like PCA (Ferreras et al. 2006) or piecewise-linear matrix inversion (Dye 2008), which need regularization to yield physical solutions.

7. *Robust to noise:* The atlas spans the space of physically motivated SFHs, but not the space of all possible SEDs. This makes it robust to noise in the sense that distortions due to noise that are not accessible through the physically

motivated families of SFHs under consideration do not bias the fits, as described in Appendix D.

We describe a few of the two-parameter families of curves for the current analysis. An overall normalization corresponding to the stellar mass acts as a third parameter. A visual representation of these families is shown in Figure 2.

1. *Top-Hat*: Historically, simple stellar populations (SSPs) assumed that a galaxy's stellar population formed in a single instantaneous burst (Tinsley 1980). An improvement over that was the extension to constant star formation (CSF) from a start time through the time of observation at a fixed rate. Here we use a two-parameter version of this parametrization, with a start time and a width.[2] This is also useful for comparison with quantities in the literature computed using CSF histories, which correspond to setting $\tau \geqslant t_{obs} - t_0$.

$$\text{SFR}(t, t_0, \tau) = \Theta(t - t_0)(1 - \Theta(t - t_0 - \tau)) \qquad (1)$$

where $\Theta(t)$ denotes the Heaviside function with $\Theta(t) = 1$ for $t \geqslant 0$ and $\Theta(t) = 0$ for $t < 0$, t_0 is the time at which star formation starts, and τ is the width of the Top-Hat.

2. *ESF*: Exponentially declining star formation rates, a parametrization that performs well for local ellipticals and for comparison with older literature, where t_0 is the time at which star formation starts and τ is the rate constant of

---

[2] Since this is a positive definite version of the Top-Hat wavelet, this illustrates the possibility of extending our method to a wavelet basis.
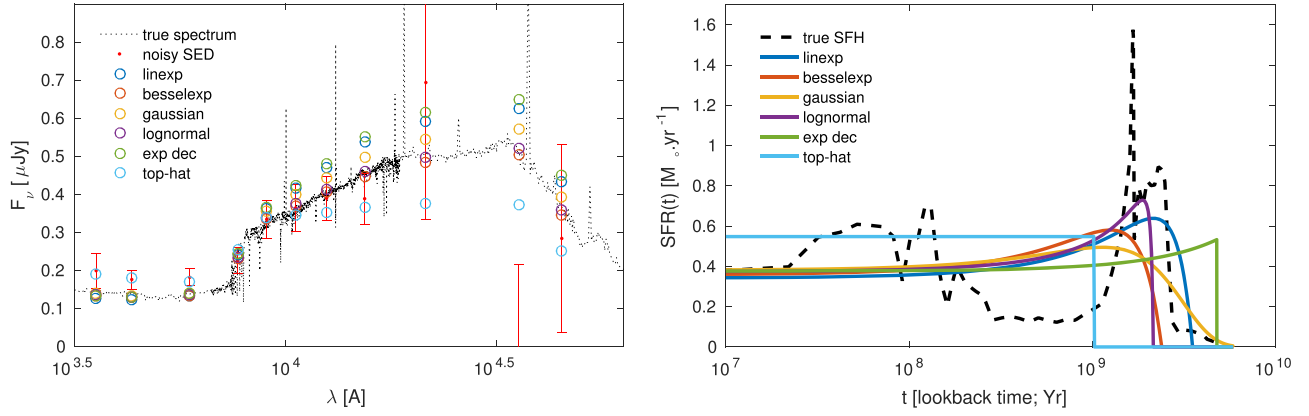
Figure 3. Reconstruction of SAM mock star formation history using the six SFH parametrizations being considered as candidates for the dense basis method. Left panel: the blue curve shows the true spectrum at $z = 1$. Red data points show the noisified SED obtained by multiplying with filter transmission curves and adding photometric noise realized from a quadrature sum of CANDELS photometric and zeropoint uncertainties (10% for the U_CTIO, Ks and IRAC ch1, 2 bands, and 3% for the remaining photometric bands: f435w, f606w, f775w, f850lp, f105w, f125w, f160w). Colored circles show the best-fit SEDs corresponding to each reconstructed star formation history. Right panel: the black dashed curve shows the SAM star formation history. Colored curves indicate SFR at a given lookback time at $z = 1$ for SFHs from each family that are best fits to the noisified SED. The top-hat parametrization underestimates the stellar mass of the galaxy by $\sim$60%, while the exponentially declining SFH overestimates the stellar mass by $\sim$46%.

the exponential decline.

$$\mathrm{SFR}(t, t_0, \tau) = \Theta(t - t_0)\exp\left(-\frac{(t - t_0)}{\tau}\right). \qquad (2)$$

3. *Linexp*: The delayed exponential (Gavazzi et al. 2002; Behroozi et al. 2010; Lee et al. 2010) with an additional parametrized start-time t_0 (henceforth *Linexp*) giving the time at which star formation starts and τ setting the width of the episode of star formation.

$$\mathrm{SFR}(t, t_0, \tau) = \Theta(t - t_0)((t - t_0)/\tau)e^{-(t-t_0)/\tau}. \qquad (3)$$

4. *Gaussian*: A parametrization that is useful for describing symmetric episodes of star formation, where t_{peak} is the time at which star formation peaks and τ is the standard deviation, which sets the width of the episode of star formation.

$$\mathrm{SFR}(t, t_{\mathrm{peak}}, \tau) = \exp\left(\frac{-(t - t_{\mathrm{peak}})^2}{2\tau^2}\right). \qquad (4)$$

5. *Log-normal*: (Gladders et al. 2013; Dressler & Abramson 2014) A two-parameter statistical distribution that appears in many physical processes, t_0 is the time at which star formation starts and τ sets the width of the episode of star formation.

$$\mathrm{SFR}(t, t_0, \tau) = \Theta(t - t_0)\frac{1}{t}\exp\frac{-(\ln(t - t_0))^2}{2\tau^2}. \qquad (5)$$

6. *Besselexp*: Bessel-function rise, followed by exponential decline (henceforth *Besselexp*). The order of the Bessel function of the first kind, ν determines when the SFR peaks,[3] and τ sets the width of the episode of star formation.

$$\mathrm{SFR}(t, \nu, \tau) = J_\nu(t/\tau)e^{-t/\tau} + \alpha t. \qquad (6)$$

We add a linear piece such that $\alpha t_{\mathrm{min}} = -\min(J_\nu(t/\tau)\,e^{-t/\tau}))$, to ensure that the set of functions described by

this family remains positive definite, while also satisfying $\mathrm{SFR}(t = 0) = 0$ at the big bang.

These functions offer the advantages of being able to model short episodes of star formation at specific times (small t) or long periods of star formation, where the rate rises and then falls (e.g., Pacifici et al. 2012; Tomczak et al. 2016). Figure 3 shows a typical SFH drawn from simulations and fits using the six families of SFHs described above. It can be seen that the standard parametrizations of constant star formation and exponentially declining star formation under- and overestimate the stellar mass of the galaxy, while the other families show an improved estimation of the general trend of star formation. Additionally, the expansion of the basis to include all physically motivated combinations of single-component SFHs will allow us to describe SFHs with multiple episodes of star formation separated by periods of relative quiescence in a galaxy's SFH.

2.2. The SED Fitting Problem: Reconstruction of SFHs

For an SSP, which assumes that all of its stars form at a single lookback time (T) and with the same metallicity (Z), the luminosity at a given wavelength (λ) is simply

$$L_\lambda = \int_{t_{\mathrm{bb}}\equiv 0}^{t_{\mathrm{obs}}} dt' L_\lambda^{\mathrm{SSP}}(t_{\mathrm{obs}} - t', Z)\delta(T - t_{\mathrm{obs}} + t')$$
$$= L_\lambda^{\mathrm{SSP}}(t_{\mathrm{obs}} - T, Z) \qquad (7)$$

where t' is the time since the big bang, $t_{\mathrm{obs}} - T$ is the age of the galaxy at t_{obs}, and $L_\lambda^{\mathrm{SSP}}(t, Z)$ is the spectrum giving the luminosity of an SSP of metallicity Z at age t since formation. The SSP spectrum contains assumptions for the IMF, stellar tracks, and metallicity, which we hold constant in the current study. Some of the effects of relaxing this assumption are noted in Section 4.3, and are discussed further in Section 6.2.

Generalizing from SSPs to composite stellar populations (CSPs), we can then represent the SED for a galaxy with a given SFH (SFH $\equiv \psi(t)$) as an integral over all of the star formation events that occurred at different times from the birth of the universe to the time of observation. CSPs are written as a sum over a non-orthogonal set of SFHs that satisfy the

---

[3] Although there is no closed form expression for this, it can be easily determined from a lookup table for the zeros of $J'_\nu(t/\tau)$, and the linear approximation is $t_{\mathrm{peak}} \sim 1.5(10^8)\nu$ year.

Table 1
Parameter Space for Vetting Using Mock SEDs

	Parameter Choice	Range
IMF	Chabrier/Salpeter	⋯
SED generation:	BC03	⋯
Bands fit	11	⋯
Tracks	Padova'94	⋯
Metallicity	$0.2\,Z_\odot$	⋯
Dust law	Calzetti	$A_\nu \in [0.0, 2.5]$, $R_\nu = 4.05$
SFH form	Linexp	$\tau \in [0.014, 138]$ Gyr, $t_0 \in [0.02, 5.9]$ Gyr
"	Gaussian	$\tau \in [0.014, 4.36]$ Gyr, $t_{\rm peak} \in [0.02, 5.9]$ Gyr
"	Besselexp	$\tau \in [1.38, 4.36]$ Gyr, $t_{\rm peak} \in [0.05, 5.66]$ Gyr
"	log-normal	$\tau \in [1.38, 4.36]$ Gyr, $t_0 \in [0.05, 5.66]$ Gyr
"	exponential	$\tau \in [0.014, 138]$ Gyr, $t_0 \in [0.02, 5.9]$ Gyr
"	top-hat	$\tau \in [0.014, 13.8]$ Gyr, $t_0 \in [0.02, 5.9]$ Gyr

constraints outlined in Section 2.1, such that

$$\psi(t) \equiv \sum_k \epsilon_k \psi_k(t, \{\tau, t_0\}) \tag{8}$$

with $\epsilon_k \geqslant 0$ denoting an overall normalization corresponding to the stellar mass formed by the SFH $\psi_k(t)$. Given a basis of SFHs that spans this space, we can expand this instead as a sum over the parameter space, akin to a Fourier expansion, as

$$L_\lambda = \sum_k \epsilon_k L_\lambda^k(\psi_k(t, \{\tau, t_0\}, Z) \tag{9}$$

where the contribution to the luminosity from an episode of star formation $\psi_k(t, \{\tau, t_0\})$ described by a family of curves from Equations (1)–(6) with the parameters $\{\tau, t_0\}$ is given by

$$L_\lambda^k = \int_{t_{\rm bb}\equiv 0}^{t_{\rm obs}} dt'\, L_\lambda^{\rm SSP}(t_{\rm obs} - t', Z)\, \psi_k(t'). \tag{10}$$

Dust reddening and nebular emission lines are then applied to the spectrum as described in Section 2.3, denoted by the notation $L_{\lambda,R}$. The photometry in passband j from the kth basis SFH $\psi_k(t)$ parametrized by $\{\tau, t_0\}$, is then given by

$$F_j^k = \frac{1}{4\pi d_L^2(1+z)}$$
$$\times \sum_k \left(\int d\lambda\, T_j(\lambda)\, \epsilon_k L_{\lambda,R}^i(\psi_k(t; \{\tau, t_0\}, Z)) \right). \tag{11}$$

Using this as a mapping from the basis of SFHs to the space of all physically motivated SEDs, we can then define a χ^2 surface, which denotes the metric distance in the vector space of photometry between the observed SED and its closest match in the atlas. Finding the reconstructed SFH in the basis is then reduced to an optimization problem on the likelihood surface. For example, with a surface defined using a χ^2 metric, we get

reconstruction in SFH space, given by Γ, defined in Section 3. We choose basis functions that show sufficient correspondence between the optima of these two quantities, which lets us reconstruct SFHs in the presence of model degeneracies, systematics, and instrumental noise.

2.3. Generating the Atlas

In order to implement the dense-basis algorithm, it is necessary to first generate an atlas of template SEDs and then to use it to fit the observed SEDs. This is done as follows.

1. Basis SFHs belonging to the functional families described in Section 2.1 are generated on a grid of well-chosen discrete parameter values.
2. SEDs corresponding to these SFHs are then generated using the isochrone synthesis code BC03. (Bruzual & Charlot 2003), using input parameter ranges as described in Table 1.
3. Nebular emission is added according to the prescription in Orsi et al. (2014) using MAPPINGS III, a one-dimensional shock and photoionization code for modeling nebular line and continuum emission. (Allen et al. 2008). We use in this work the precomputed H II region model grid described in Kewley et al. (2001), with the incident ionization spectra computed using Starburst 99 (Leitherer et al. 1999), at $Z_{\rm cold\ gas} = 0.2\,Z_\odot$, from which we compute the ionization parameter using

$$q(Z) = 2.8 \times 10^7 \left(\frac{Z_{\rm cold}}{0.012} \right)^{-1.3}. \tag{13}$$

This prescription does not add effective degrees of freedom to the atlas and could be expanded to accommodate more realistic emission in future work with higher S/N SEDs.

$$\min(\chi^2) = \min \left[\sum_j \frac{\sum_k \left[(4\pi d_L^2(1+z))^{-1} \int d\lambda\, T_j(\lambda)\, \epsilon_k L_{\lambda,R}^i(\psi_k(t; \{\tau, t_0\}, Z) - F_j^{\rm obs} \right]^2}{\sigma_j^2} \right] \tag{12}$$

In the following sections, we train the basis set using different mock data sets for which we can quantify both the goodness-of-fit in SED space, given by χ^2 as well as the goodness-of-

4. Calzetti Dust Attenuation (Calzetti 2001) is applied to atlas SED spectra with discrete values of A_ν to extend parameter space in dust for procedures where dusty SEDs

are fit, using

$$L_{\lambda,R} = L_\lambda 10^{-0.4k(\lambda)A_V/R_V} \qquad (14)$$

where

$$
\begin{aligned}
k(\lambda) &= 2.659\left(-2.156 + \frac{1.509}{\lambda} - \frac{0.198}{\lambda^2} + \frac{0.0011}{\lambda^3}\right) \\
&\quad + R_V \qquad \lambda \in [0.12, 0.63] \\
&= 2.659\left(-1.857 + \frac{1.04}{\lambda}\right) \\
&\quad + R_V \qquad \lambda \in [0.63, 2.2]
\end{aligned}
$$

with $R_V = 4.05$ and the coefficients adjusted for λ in microns. Since attenuation inferred from nebular emission lines differs from that inferred from the continuum (UV spectral slope), we use $A_{v,\mathrm{stars}} = 0.44 A_{v,\mathrm{gas}}$ (Calzetti 2001), where $A_{v,\mathrm{gas}}$ is applied to both UV nebular continuum and nebular emission lines.

5. After nebular emission lines are added to the spectrum and dust attenuation is applied, the photometry for the basis SEDs F_j^k, where j denotes the photometric bands, or spectroscopic bins, at a redshift z is given by

$$F_j(\lambda) = \frac{1}{4\pi d_L^2(1+z)} \int d\lambda\, T_j(\lambda) L_{\lambda/(1+z),R}(\psi_k(t; \{\tau, t_0\}), Z) \qquad (15)$$

where T_j is the transmission curve of passband j (the spectroscopic equivalent would be the resolution element $\Delta\lambda$ and throughput at that λ), and d_L is the luminosity distance (a d_L of 10 parsecs is assumed when $z = 0$, as in BC03). For convenience, the flux densities are obtained as the ratio of the number of photons corresponding to the fluxes (λF_λ) to the number of photons produced by a 1 μJy flat spectrum in passband j. This yields the observations, predictions, and uncertainties in identical units. The notation $L_{\lambda,R}$ indicates that nebular emission and dust reddening have been applied to the spectrum.

2.4. Choosing the Number of Basis Functions

In practice, galaxies rarely have sufficiently smooth SFHs to be perfectly fit by a functional form, as inferred from our mock data sets as well as Hammer et al. (2005), Kelson (2014), Weisz et al. (2011), Sparre et al. (2015), and Diemer et al. (2017). In addition, considering the errors in the photometry, incomplete empirical knowledge of the mapping from SFH to SED spaces, and degeneracies between the SFH and other factors like dust and metallicity, we need to assess methods of reconstruction using multiple basis SFHs to reconstruct as close to the true SFH as possible given the quality of available data. Considering a solution to the minimization problem in Equation (12), we can express the best-fit SED as

$$F_j^{\mathrm{obs}} = \sum_{k=1}^{N_{\mathrm{basis}}} \epsilon_k F_j^k(\psi_k(t)) \approx \sum_{k=1}^{N_F} \epsilon_k F_j^k(\psi_k(t)) \qquad (16)$$

where N_F is the number of components determined using the F-test, given by

$$\mathcal{F}(\chi^2_{N_1}, \chi^2_{N_2}) = \frac{(\chi^2_{N_1} - \chi^2_{N_2})/(d_2 - d_1)}{\chi^2_{N_2}/d_2}$$
$$\text{reject if } p(\mathcal{F}, d_1, d_2) < 0.5. \qquad (17)$$

This is used to determine the number of components in the SFH space that the SED should be fit with. The F-test assesses the null hypothesis that the fit with a larger number of parameters is not a statistical improvement over a fit with a smaller number of parameters,[4] where $d_2 = N_j - 3N_2$, $d_1 = N_j - 3N_1$ are degrees of freedom corresponding to the number of components (N_1, N_2) being fit, with N_j denoting the number of photometric bands.

We then reconstruct the SFH according to the optimal components of the likelihood surface for the chosen N_f.

2.5. Estimating Uncertainties

We estimate uncertainties for the reconstructed SFHs via a fully forward modeled frequentist approach using the likelihood surface of the fit, after rescaling the best-fit χ^2 to correct for artificially low χ^2 obtained for very noisy galaxies and artificially high χ^2 values for the brightest galaxies.

A subsurface of the complete likelihood surface is then obtained by imposing a cutoff using a procedure similar to that of (Avni 1976). We compare the SFH corresponding to each point in the subsurface to the median SFH and exclude outlier SFHs that have an excursion greater than 1.5 times the maximum value, yielding robust confidence intervals as in Xie & Singh (2013) and Zhao & Ma (2016). The uncertainties in SFR at each point in time are then found using a distribution of the remaining acceptable SFHs. Our tests using the sample of 1200 mock SFHs show that this method robustly estimates the confidence bounds, such that, for a formal 68% confidence interval, the true SFH lies within the confidence interval $\sim$79% of the time. We show the χ^2 surface computed using this procedure for a single family in Figure 4, showing the best-fit SFH and threshold for uncertainties. In Figure 5, we show some representative examples of the uncertainties with the top panel demonstrating the method's ability to constrain an older episode of star formation and the bottom panel showing the case of uncertainties with multiple episodes of star formation.

2.6. Choice of Parameter Space and Photometric Bands

For the initial implementation of the method in this work, we have used the Bruzual & Charlot (2003) library of stellar tracks, with the parameter space as described by Table 1. The Dense Basis formalism can be applied equivalently with any set of free parameters, including the set of SSP models, to use the training and validation steps to help constrain the variable parameters, as discussed in Section 6.2. All three data sets are standardized to contain a sample of 400 galaxies with the same realistic distribution of stellar mass.

---

[4] To motivate the choice of $p = 0.5$ as our bounding value, it helps to think of the case with an equal number of degrees of freedom ($N_1 = N_2$), where a better statistical model has $F > 1$, which corresponds to $p > 0.5$. For the general case of $N_1 \neq N_2$, the $p > 0.5$ cutoff provides a metric where statistical improvement is sufficient to justify the extra degrees of freedom.
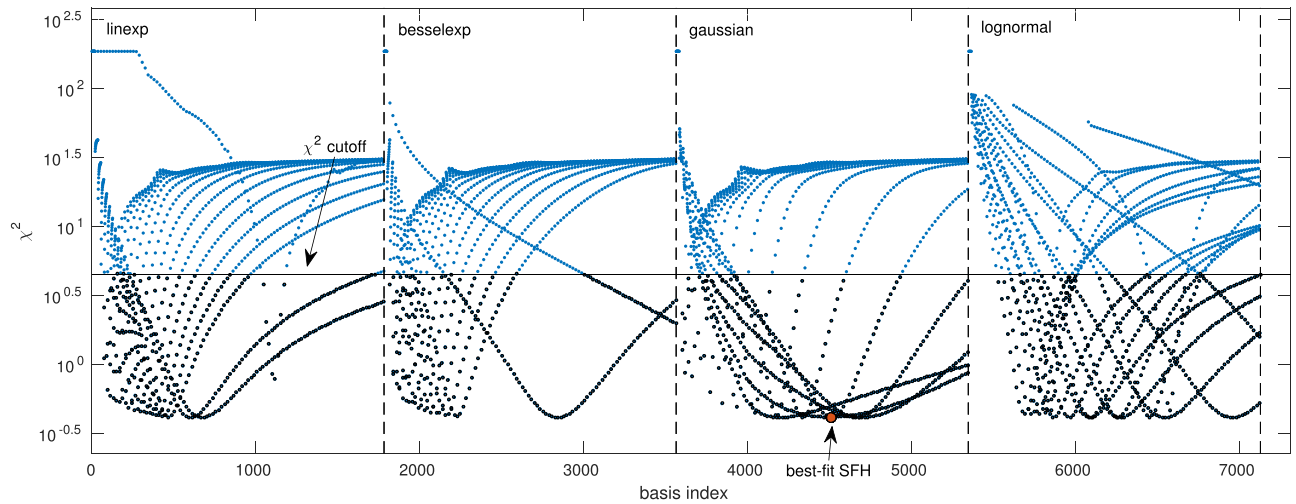
Figure 4. Plot showing the full χ^2 surface for an individual SAM galaxy, computed using the single component basis consisting of the Linexp, Besselexp, Gaussian, and Log-normal families of SFHs. Each point represents a single SFH; the SFH corresponding to the global minimum χ^2 is the best-fit SFH and SFHs from all families below a threshold are used in computing the uncertainties on the reconstruction. The curves seen within each family denote χ^2 for different values of τ with adjoining points differing by $\Delta t_0 \sim 0.1$ dex.

For training and validation, we consider fitting 11 of the 17 CANDELS GOODS-S (Guo et al. 2013) bands: [u_ctio, *HST*/ ACS F435w, F606w, F775w, F850lp, *HST*/WFC3 F105w, F125w, F160w, VLT/HAWK-I Ks, and *Spitzer*/IRAC 3.6, 4.5 μm], excluding *u_vimos*, F814w, F098w, and Isaac Ks for the maximum photometric orthogonality, excluding IRAC 5.8 and 8.0 μm since the BC03 tracks do not account for the PAH emission that appear in those bands at $z = 1$. Once the method was tested, we expanded to include the u_vimos, F814w, F098w, and Isaac Ks bands as well, leading to fits using 15-band photometry in Section 4.2. The training is performed on the mock data sets described in Section 3, the validation is performed using both the mocks data sets as well as the CANDELS sample for which SpeedyMC results are available. Finally, the results are compiled using the full CANDELS sample at $1 < z < 1.5$.

We present results at $z = 1$ in the current work since it allows us to analyze rest-UV information that comes into the *UBV* bands as well as the Balmer 4000 A break, while avoiding dust re-emission in the mid-IR. This choice of redshift and filter set is compatible with the BC03 SPS models while providing a moderate S/N regime in which to test the reconstruction of SFHs. The procedure can be generalized to all redshifts and is discussed in Section 6.3.

3. Training the SFH Families

To inform the choice of a functional form for the SFH basis, we train and validate the method with three mock data sets

To inform the choice of a functional form for the SFH basis, we train and validate the method with three mock data sets of 400 galaxies each, drawn from semi-analytic models (SAMs), hydrodynamical simulations, and stochastic realizations of SFHs. We work with multiple data sets to minimize the effect of any single training set on our choice of SFH families. Using these three mock catalogs, we look at various families of two-parameter curves, and their combinations, to find the families that perform best at reconstructing SFHs. The atlas generated using that basis is then used to fit the real catalog. Before we go

into the details of the training procedure, we first briefly describe the three data sets being used.

3.1. Training with SAMs

The first data set is drawn from mock catalogs with known realistic SFHs from state-of-the-art SAMs (Somerville et al. 2015). These simulations use dark matter halo "merger trees" extracted from dissipationless *N*-body simulations in a ΛCDM universe (Klypin et al. 2011) to determine the masses of dark matter halos collapsing at a given epoch, following which halos merge to form larger structures. In this framework, SAMs use analytic recipes to model the radiative cooling of gas, suppression of gas infall, and cooling due to the presence of a photoionizing background, collapse of cold gas to form a rotationally supported disk, conversion of cold gas into stars, and feedback and chemical enrichment from massive stars and supernovae. A more recent generation of SAMs also includes prescriptions for the growth of supermassive black holes and the impact of the energy they release on galaxies and their surroundings (Bower et al. 2006; Croton et al. 2006; Somerville et al. 2008). Recent comparisons have shown that SAMs produce similar predictions for fundamental galaxy properties to those of numerical hydrodynamic simulations, perhaps because of the common framework of ΛCDM, which dictates grav-itationally driven gas accretion rates (Somerville et al. 2015). However, SAMs require orders of magnitude less computing time for a given volume than hydrodynamical cosmological simulations. The resulting galaxy star formation and enrichment histories are outputs. We then use these SFHs to produce SEDs to train and validate against, using a realistic mass distribution of galaxies with $M_* \geqslant 10^9 \, M_\odot$.

3.2. Training with Hydrodynamic Simulations

We also train the method against a set of SFHs obtained from the MUFASA meshless hydrodynamic simulations (Davé et al. 2016), which satisfies multiple observational constraints like the stellar mass—halo mass relation (Behroozi et al. 2013; Munshi et al. 2013), the mass–metallicity relation (Steidel
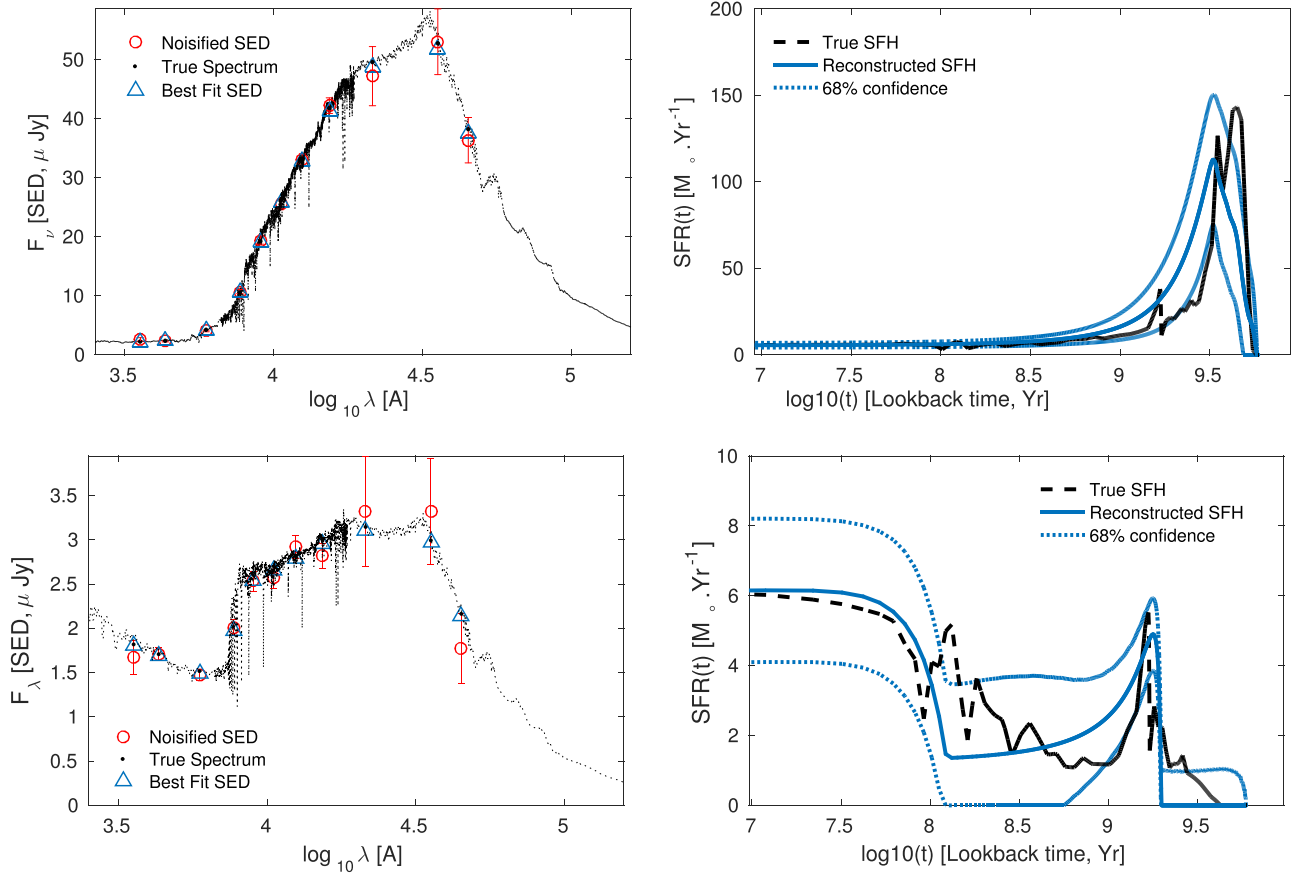
Figure 5. Representative examples of SFH reconstructions with the uncertainties computed using the outlier-clipped likelihood surface, as described in Section 5.4. The examples show that it is possible to reasonably constrain even older episodes of star formation (top row), as well as to obtain robust uncertainties on multiple episodes (bottom row). Spectra are shown without nebular emission for clarity.

et al. 2014; Sanders et al. 2015), and the SFR–M_* relation (Speagle et al. 2014; Kurczynski et al. 2016). The SFHs are reported as instantaneous star formation events that take place, ranging from $\mathcal{O}(10)$ to $\mathcal{O}(10^5)$ events for different galaxies. We restrict the fits to galaxies with $M_* \geqslant 10^9\,M_\odot$, which have well-defined SFHs in the simulation. To ensure that the SFHs are not artificially stochastic, we generate the SFHs by convolving the instantaneous star formation events using an Epanechnikov kernel with a width of 100 Myr (R. Dave, 2017, private communication) The galaxies in MUFASA follow a realistic mass distribution that we use to sample all three mock data sets. We restrict the fits to galaxies with $M_* \geqslant 10^9\,M_\odot$, which have well-defined SFHs in the simulation.

3.3. Training with Stochastic SFHs

Following the prescription of Kelson (2014), we generate stochastic SFHs with different values for the Hurst parameter H, which quantified the autocorrelation of the SFH. A value of $H = 0.5$ corresponds to a random walk in $\Delta \text{SFR}/\Delta t$, $H > 0.5$ is correlated and $H < 0.5$ is anti-correlated (Mandelbrot & Van Ness 1968). This provides a sample for testing the other families against to determine possible biases. We generate different SFHs by varying the Hurst exponent, which encodes the long-time correlation of the stochastic SFHs in $H \in [0.5, 1]$, sampling galaxies with the same mass distribution as the SAM and hydrodynamic SFH samples. We exclude from the sample SFHs

with a Hurst parameter $H < 0.5$ since these do not correspond to realistic looking SFHs.

3.4. Training Procedure and Results

We quantify the correspondence between the goodness-of-fit in SED space and the goodness-of-reconstruction in SFH space as a metric to judge the success of each family of basis functions. For the SED goodness-of-fit, we use χ^2_{SED}, given by

$$\chi^2_{\text{SED}} = \sum_j \frac{\left(\sum_{k=1}^{N_F} \epsilon_k F_j^k - F_j^{\text{obs}}\right)^2}{\sigma_j^2} \quad (18)$$

where the index k sums over the entire basis of SFHs, with a number of components determined using the F-test as described in Section 2.4 and the index j sums over the photometric bands. The ϵ_k is optimized for each basis function, effectively making stellar mass the normalization. The global minima of the χ^2 surface corresponds to the maximum likelihood, given by $\mathcal{L} \propto e^{-\chi^2_{\text{SED}}/2}$.

To quantitatively compare how well the families perform at reconstructing the SFHs of the galaxies in the three mock catalogs, we quantify the accuracy of reconstruction of the SFH by computing the R^2 statistic, given by

$$R^2(\psi_{\text{true}}, \psi_{\text{rec}}) = 1 - \frac{\sum_t (\psi_{\text{true}}(t) - \psi_{\text{rec}}(t))^2}{\sum_t (\psi_{\text{true}}(t) - \langle \psi_{\text{true}}(t) \rangle)^2} \quad (19)$$
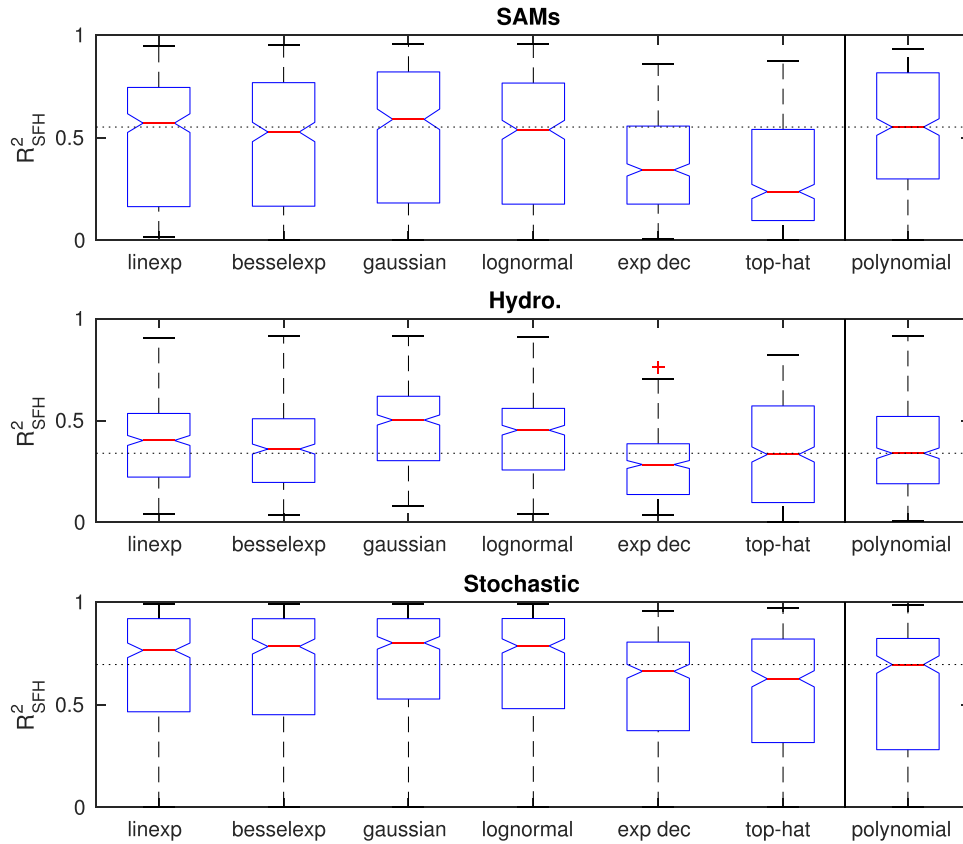
Figure 6. Boxplots showing the accuracy of reconstruction of each SFH family to each mock data set using the R^2 statistic, with the red line denoting the median and the box denoting the interquartile range. For reference, we also show the R^2 from direct polynomial fits to the SFH, with its median forming the horizontal dotted line. We see that, on average, fits to the SEDs using the Linexp, Besselexp, Gaussian, and Log-normal families perform as well as, or better than, direct fits to the SFHs with third-order polynomials.

where R^2 (Anderson-Sprecher 1994) quantifies the amount of variance explained by the fit. We set an ambitious goal for the reconstruction by asking if it does as well as direct fits in SFH space to the true SFHs using polynomials of the same order. Since the true SFHs exhibit a large amount of stochasticity, the question of good R^2 due to overfitting does not usually occur and is handled by the F-test in Section 4.1. We define the R^2 statistic in logarithmic time; since the SED is sensitive to changes in the SFR over roughly equal logarithmic intervals of time, this provides a more sensitive estimator. To handle all three data sets on the same footing, since they contain SFHs with differing amounts of structure and stochasticity, we apply a small nonparametric smoothing (Cleveland 1979) to the SFHs. This statistic has proved to be the most robust for the current application, matching the qualitative results with other statistics, as detailed in Appendix C. R^2 ranges from [0, 1], with the most successful reconstruction given by $R^2 \rightarrow 1$.

In the noiseless regime, most galaxies show the expected correspondence between the goodness-of-fit and goodness-of-reconstruction, especially in the regime of high likelihood $(\chi^2_{SED}/\mathrm{dof} < 1)$. Since we can access only χ^2_{SED} observationally, this correspondence is important since it allows us to obtain a good reconstruction for a galaxy whose SED is well fit. In order for an SFH family to be robust, we require that the SFHs for the ensemble of galaxies should be reconstructed as well as possible, comparing with direct fits to the true SFH using a polynomial with the same number of degrees of freedom.

In Figure 6, we show the R^2 computed for each mock data set using all six SFH families, showing that the Linexp, Besselexp, Gaussian and Lognormal families perform better overall at SFH reconstruction in comparison to the traditional parametrizations of constant and exponentially declining SFHs. On the basis of this, we prune our basis SFH set to retain only the Linexp, Besselexp, Gaussian, and log-normal families, hereafter denoted as "Best4 basis," to be used in further work.

As an additional step of validating our training statistic, we examine the correspondence between $\min(\chi^2_{SED})$ and a related statistic, $\min(\chi^2_{SFH})$, computed using the uncertainties obtained through the method outlined in Section 2.5 and in Appendix E. We also study the possible biases that could arise in the reconstruction with a particular family, and how our choice of basis mitigates them.

4. Validation

4.1. Validation Using Three Data Sets: Hydrodynamic Simulations, Semi-analytic Models and Stochastic SFHs

Having trained our method to arrive at an optimal basis for the data set in consideration, we now apply the SED Fitting method to the full sample of 1200 SFHs drawn from the hydrodynamic simulation, SAM, and the stochastic realizations.

Realistic simulated photometric noise has been applied to the mock SEDs to simulate observing conditions. The noise consists of a multiplicative factor corresponding to the zeropoint uncertainty in each band: 3% for the space-based bands,
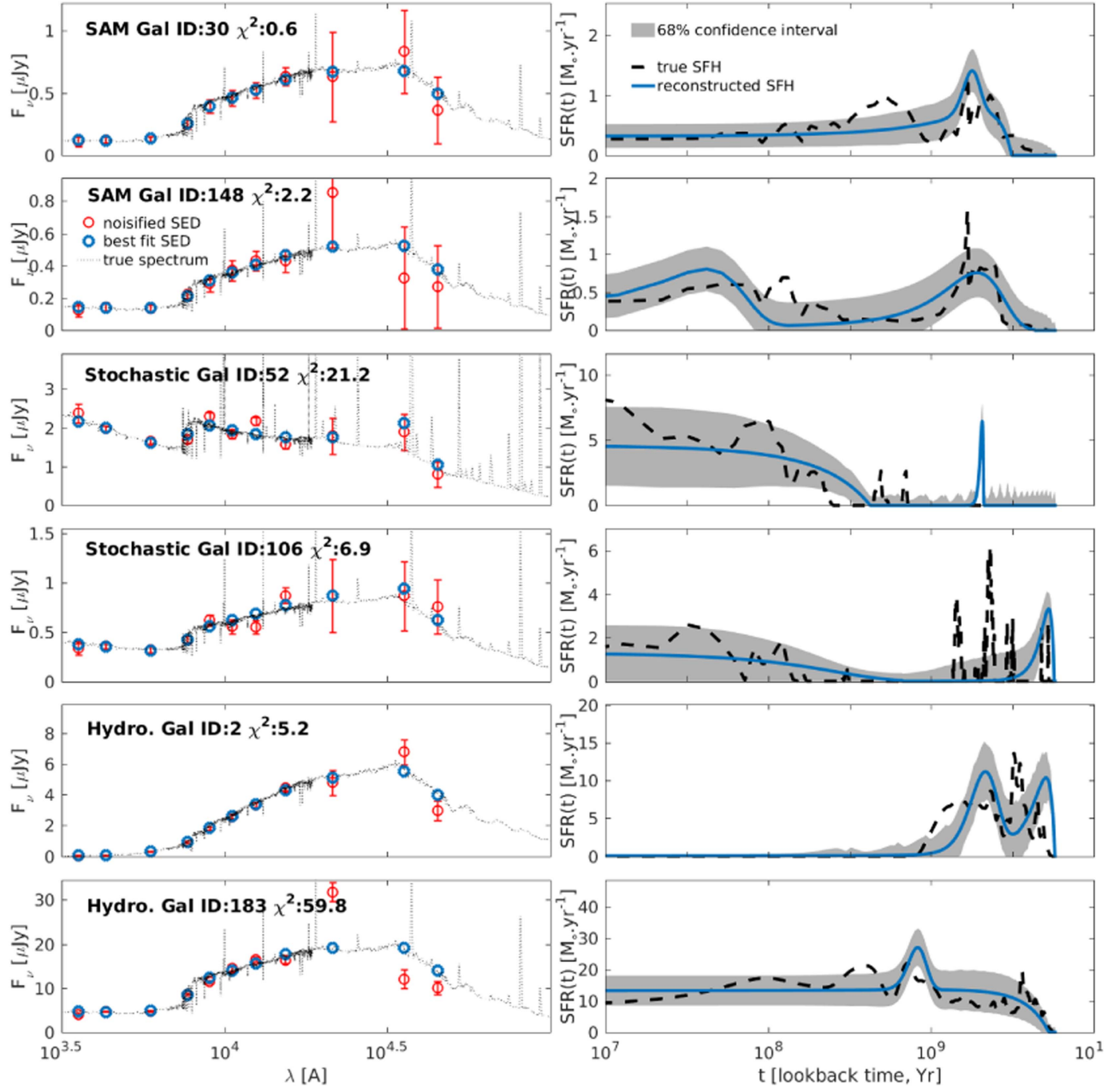
Figure 7. The plots show a randomly drawn sample from the semi-analytic models (top rows), stochastic realizations (middle rows), and hydrodynamic simulations (bottom rows) used for the training and validation of the dense basis method, showing individual examples from the ensemble results shown in Figure 8. Left: plots show the true spectrum (black line) from the mock catalogs, their corresponding noisified photometry (red error bars), and the best-fit SED (blue open circles) using the dense basis method. Right: plots show the true SFH (black dashed line) and its reconstruction (blue solid line) with 68% confidence intervals (gray shaded region) computed using the method described in Section 2.5. SAM galaxy 30 is identified as a one episode galaxy in the current realization of noise, constituting a false negative result of the F-test. However, many noisy realizations allow us to currently identify the second episode at $t \sim 6e8$ years. The episodes of star formation for the hydro. galaxy 2 is distorted either due to noise or dust. The additional peaks in Stochastic galaxy 106 and hydro. galaxy 183 require a basis with more components.

(HST/WFC3 and HST/ACS) and 10% for the ground-based bands (U ctio, U vimos, Isaac Ks, HawkI Ks) and IRAC Ch.1–4, as well as a photometric additive factor corresponding to the median errors in each band computed from the CANDELS data set. With these added in quadrature to yield the σ_i for each band i, simulated fluxes were drawn from a Gaussian distribution $\mathcal{N}(F_\nu^i, \sigma_i^2)$.

We show fits using the Best4 basis that is a combination of Linexp, Besselexp, Gaussian, and log-normal families, as was determined through the training step in Section 3.1. The galaxy SEDs have been fit with an atlas consisting of two component

basis SFHs. This basis is constructed using all physical combinations of elements from the single episode basis and is seen to have a smaller scatter around the true values, as described in Section 6.1. In Figure 7, we show the reconstructed SFHs for two randomly selected galaxies from each mock data set, illustrating the recovery of both recent episodes of star formation, as well as the overall trend of star formation, including periods of relative quiescence.

In Figure 8, we illustrate the recovery of four physical quantities: the stellar mass (M_*), the star formation rate averaged over the last 100 Myr (SFR$_{100}$), the lookback time
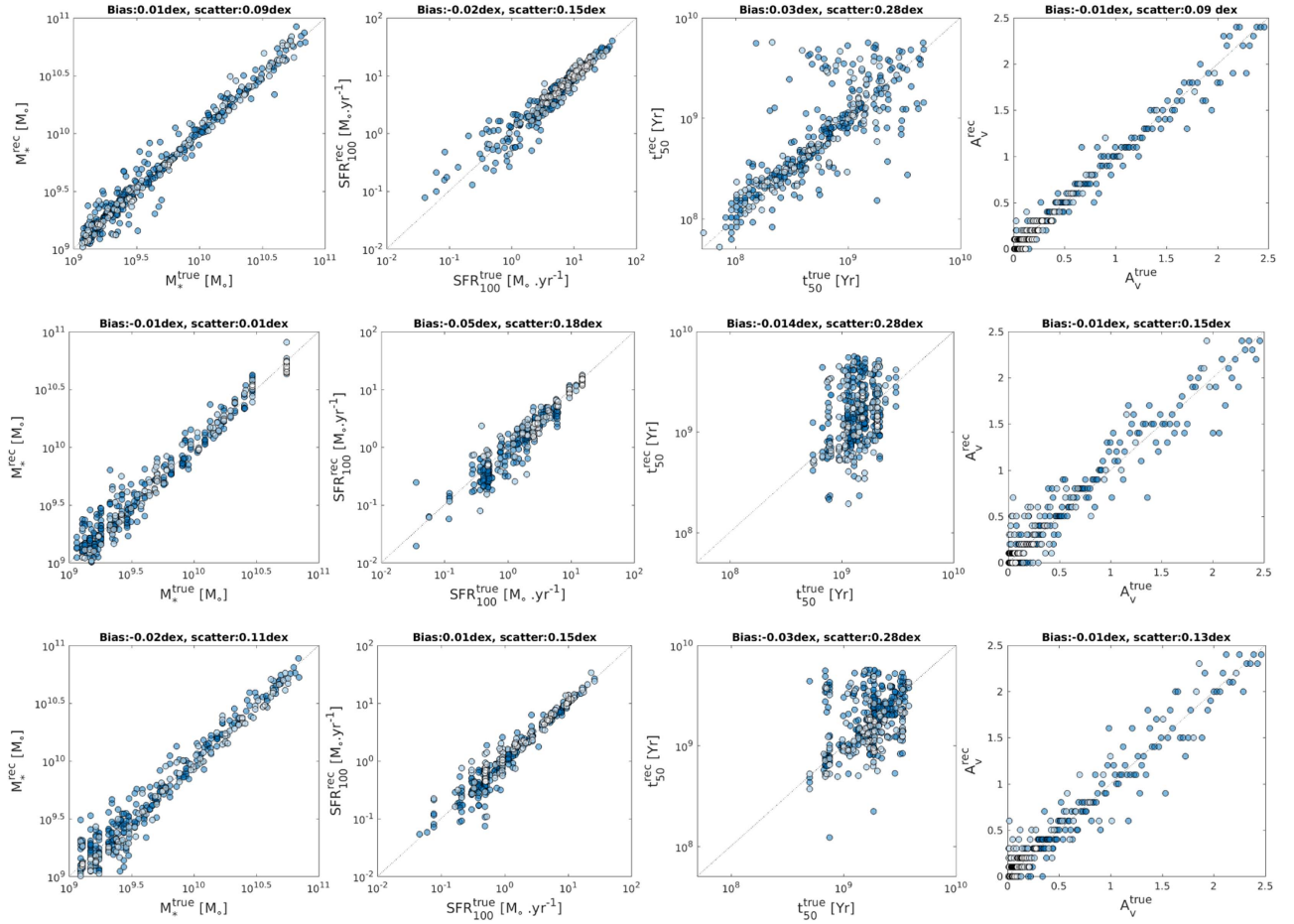
Figure 8. We show the comparison of reconstructed against true values of the stellar mass (M_*), SFR$_{100}$, and t_{50} for three data sets: the stochastic realizations (top row), MUFASA hydrodynamic simulations (middle row), and Semi-Analytic Model SFHs (bottom row), using the 2 episode Best4 basis fit using the dense basis method. For each data set, we use a sample of 400 galaxies drawn from a realistic mass distribution. The shading indicates the likelihood of the fit, with darker shades denoting better fits to the SED.

over which the galaxy accreted 50% of its observed stellar mass (t_{50}), and dust extinction (A_v). The top row depicts the results for the stochastic realizations, the middle row for the hydrodynamic simulations, and the bottom row for the SAMs. All of the fits show the bias to now be significantly smaller than the scatter that may occur from using a single family of SFHs, as discussed in Section 6.1. The scatter in stellar mass increases at lower mass, corresponding to more noisy SEDs, while the increased scatter in SFR as compared to the values in Section 6.1 is more due to the presence of dust than noise since fits without dust show a much smaller scatter of ∼0.05 dex. The 0.3 dex scatter in the reconstruction of t_{50} is reasonable. However, the distributions for the SAMs and the hydrodynamic simulations look poor due to the narrow range of true values for these models with the top row being more representative of the method's performance with a broader distribution of t_{50}. Reconstruction of simulated dust drawn from an exponential distribution is done using an atlas containing 25 values of dust ranging from $A_v = 0$ to $A_v = 2.5$ using the Calzetti dust law, with a reasonable scatter of 0.09–0.13 dex and negligible bias of ∼0.01 dex.

We find that our choice of basis yields comparably good results to all three mock data sets, with the bias in the estimation of these physical quantities derived from the SFH not exceeding 0.05 dex, as seen in Figure 8. This is an important criterion to be met before the method is applied to observational data, since it lets us relax the assumption that the SFHs corresponding to the training SEDs match the actual SFHs of galaxies at a given epoch, in favor of the slightly weaker assumption that the SFHs are drawn from a similar distribution. The ensemble results show that the reconstruction is nearly unbiased for the physical parameters of interest and can be used to extract a variety of derived quantities from the SED of distant galaxies in a robust manner.

We also present results in Figure 9 for the fraction of a sample of galaxies that are reconstructed with a second episode of star formation. For our three data sets, we perform the F-test using Equation (18), with $N_1 = 1$, $N_2 = 2$, and obtain the fraction of galaxies that are significantly better fit with a second component of star formation. In some cases, the second component has similar peak time and serves only to modify the SFH shape, e.g., Gaussian + log-normal, with a single peak; we term these single episode SFHs. We then find the fraction of the mock galaxies that have a distinct second peak to their reconstructed SFH, which can only happen when the reconstruction prefers a second component. We compare this number to the number of galaxies in the sample whose true SFH has two episodes of star formation, computed using a peak finding routine. Since the true SFHs show a large amount of stochasticity, only the most prominent peaks with a separation
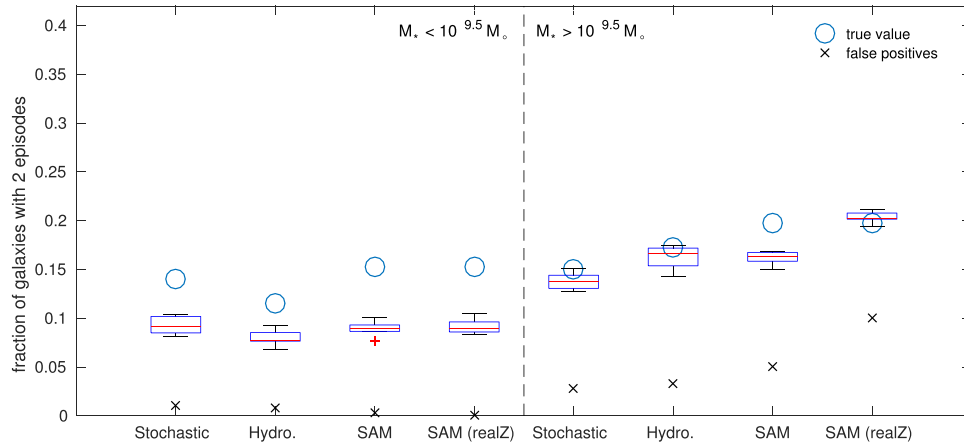
Figure 9. We find the number of galaxies that show a statistical improvement upon being fit with a second component of star formation using the Best4 basis from Section 3.1, determine which of those correspond to a second episode of star formation, and present results for noisy realizations of four data sets of galaxies from the hydrodynamic simulations, stochastic realizations, Semi-Analytic Model, and the realistic metallicity generalization of the Semi-Analytic Model described in Section 4.3. The blue values are obtained directly from the true SFHs using a smoothing algorithm to account for stochasticity and then running a peak finder algorithm, while the black crosses quantify the number of false positive predictions using the F-test. The results are divided into two mass bins, showing that the method is reliable in predicting the number of episodes at the high-mass end, due to sufficient S/N.

greater than 100 Myr are selected by smoothing over the local variations as in Section 3.1 and finding the lookback times at which the SFH peaks, using $SFR'(t) = 0$ and $SFR''(t) < 0$. The results are summarized as boxplots in Figure 9, for two mass bins chosen such that roughly half the sample lies in each mass bin. For the high-mass bin, the higher S/N leads to more accurate predictions of the fraction of SEDs with more than one episode of star formation. Since our atlas is restricted to SEDs corresponding to physically motivated SFHs, we generally do not overfit the noise, as is seen by the small number of false positive results.[5] However, a large amount of noise makes it more difficult for the F-test to detect a statistically significant improvement to the fit. This leads to a systematic under-estimation of the fraction of galaxies with more than a single episode of star formation, as shown in our results for the lower-mass galaxies. The decreased S/N also results in the fraction of fits with false negatives[6] being higher in this mass bin.

4.2. Validation Against SpeedyMC Results for CANDELS SEDs

We now apply the method to a sample of 1100 CANDELS galaxies in the GOODS-S field at $1 < z < 1.5$ from Kurczynski et al. (2016), for which we have physical quantities derived using SpeedyMC[7] (Acquaviva et al. 2011, 2015) for 742 galaxies. This sample provides a good representative redshift to test the method for the recovery of SFHs at moderate S/N, as discussed toward the end of Section 2.6. We perform the fitting with discrete values for z and A_v, which adds some scatter to the results. For redshift, we choose bin edges at [1.0, 1.1, 1.2, 1.3, 1.4, 1.5], and we let A_v vary from 0 to 2.5 in increments of 0.1. The purpose of this comparison is to ensure that our SED fitting code, developed to implement the dense basis method, which was also used to generate mock SEDs, does not contain circular errors. Additionally, it is a useful test

---

[5] Excluding the SAM (realZ) results, which we discuss further in Section 4.3.
[6] Which can be expressed as $f_{fn} \sim f_{true} - f_{rec} - f_{fp}$, where f_{fn}, f_{fp} are the fractions of false negatives and positives, and f_{true}, f_{rec} are the true and reconstructed fractions of galaxies with multiple episodes of star formation.
[7] A much faster version of the GalMC Markov Chain Monte Carlo algorithm (Acquaviva et al. 2011) is available: http://www.ctp.citytech.cuny.edu/~vacquaviva/web/GalMC.html.

Table 2
Comparison of Dense Basis and SpeedyMC
Parameter Spaces Used in Section 4.2

	Dense Basis	SpeedyMC
IMF	Salpeter	Salpeter
GoF:	χ^2	χ^2
SPS:	BC03	BC03
Bands fit	$\leqslant 17$	$\leqslant 17$
Metallicity	$0.2\,Z_\odot$	$0.2\,Z_\odot$
Dust law	Calzetti	Calzetti
Nebular emission	MAPPINGS III	custom
SFH form	Linexp	Linexp

to match the physical quantities that can be recovered through traditional SED fitting before presenting previously inaccessible quantities.

In order to make the comparison as consistent as possible, we match the initial conditions of the fitting procedure to the SpeedyMC parameter space, as summarized in Table 2, and limit our SFH basis to single-component Linexp curves. In Figure 10, we show the results comparing our fits to the SpeedyMC results for the stellar mass (M_*), SFR_{100} and t_{50}. The slight bias in t_{50} could be due to the difference in the way the two codes implement nebular emission. The colorbars denote the spectroscopic redshifts corresponding to the observed galaxies.

4.3. Validation Against SAM SEDs with Multiple Metallicities

We address a final possible source of systematic bias in the fits: the assumption of a single metallicity ($0.2\,Z_\odot$) in building the atlas and performing the fits at $z \simeq 1$. To take into account the distribution of metallicities found in real galaxies, we go back to the SAM SFHs and consider the individual metallicity components of the overall SFHs. We generate spectra corresponding to each of these metallicities using six values of metallicity available for the Padova'94 tracks in BC03, given by $Z = [0.0001, 0.0004, 0.004, 0.008, 0.02, 0.05]$. Using this procedure, we obtain spectra corresponding to the SFH in each metallicity bin and use a weighted sum to obtain SEDs
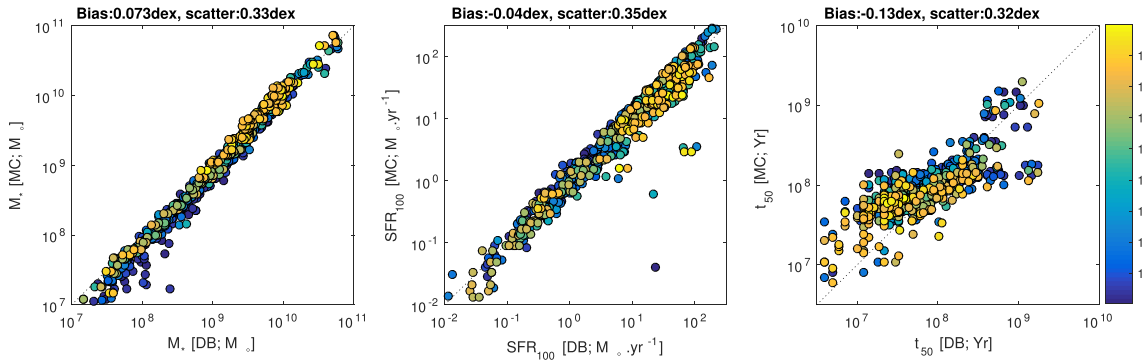
Figure 10. Comparison of physical quantities derived through the Dense Basis fits against the results of the SpeedyMC Markov Chain Monte Carlo code applied to the CANDELS data set at $1 < z < 1.5$ from Kurczynski et al. (2016), comparing the stellar mass (M_*), star formation rates, and the lookback time at which the galaxies accumulated 50% of their observed mass (t_{50}). The color table indicates the redshifts of the galaxies being fit.

corresponding to galaxies with realistic metallicity histories, which we denote as SAM (realZ). We then fit these SEDs with our single-metallicity basis to test how robust our fits are at $z = 1$.

In the left panel of Figure 11, we show the distributions of observed metallicities at $z \simeq 1$ in the SAMs, weighted using the dominant contribution to the total mass of the galaxy for realistic sampling in stellar mass (M_*) used in Section 4.1. Upon examining the SEDs corresponding to a sample of galaxies of different ages generated by combining the spectra corresponding to the SFHs in each of BC03's six metallicity bins, we find that older, more massive galaxies are more metal-rich at the observed epoch and thus show a greater deviation from the template SEDs, which currently assume $Z = 0.2 \, Z_\odot$ for the entire SFH.

In the four panels to the right of Figure 11, we show the reconstruction of physical quantities (M_*, SFR_{100}, t_{50}, and A_v) for the cumulative SEDs with realistic metallicities. The increased bias in the t_{50} appears to be the result of poorly fitting older galaxies, which have much higher metallicities than those in the atlas. For $t_{50}^{true} \sim 3 \, Gyr$ and older, galaxies tend to have $Z > 0.4 \, Z_\odot$ at the time of observation. This effect, in addition to the narrow distribution of true t_{50}, causes the scatter in t_{50} to appear poor even though it is comparable to the fits in Section 4.1. The recovered SFHs themselves are still representative of the true SFH of the galaxy up to a lookback time of $\sim 3 \, Gyr$, after which the degeneracies in the χ^2 surface due to the contributions from older stars, dust, and differing metallicities impose larger uncertainties on the reconstruction by a factor of ~ 1.22.

In Figure 9, we now focus on the results in the last columns in each mass bin. The results agree well in the high-mass bin, due to roughly equal numbers of false negatives and positives. The net results in both mass bins are still acceptable, as a result of which the method is still valid even in its current simple realization with a single metallicity.

5. Results

The dense basis method of SED fitting allows us to reconstruct the SFHs of galaxies in a nonparametric fashion, not being restricted to the choice of a particular number or family of basis SFHs, while being able to compress the reconstructed SFHs using a small number of parameters to describe a best fit. We show the results of applying this method

to our sample of CANDELS galaxies at $1 < z < 1.5$ and mock SAM galaxies at $z \sim 1$.

5.1. Going Beyond "Age" and Instantaneous SFR

The "age" of a galaxy, defined as the lookback time at which the galaxy first started forming stars ($\equiv t_0$), is not as meaningful with realistic SFHs as it used to be with SSPs, which formed all their stars at a single lookback time, given by the age (Tinsley 1980; Bruzual & Charlot 2003). Realistic SFHs as seen in the SAM and the hydrodynamic simulations may maintain a small amount of star formation before ramping up to a major episode of star formation, which results in the true age for most galaxies approaching the age of the universe. Since the SED of a galaxy is most sensitive to its largest episodes of star formation, with its sensitivity decreasing as we go back in lookback time, the "age" recovered through SED fitting methods is not a robust physical quantity. However, if we were to estimate the lookback time at which the galaxy accumulated the first 10% of its observed stellar mass, we estimate the lookback time at which any major star formation activity in the galaxy started. While the distributions of the age and t_{10} are similar for a given sample of galaxies, the latter is a more meaningful quantity in terms of studying galaxy growth and evolution and is more robustly estimated through SED fitting (Pacifici et al. 2015, 2016). This can be seen from the top panels of Figure 12, with the right panel showing noiseless reconstructions of the age, and the left panel showing noiseless reconstructions of t_{10} for all three samples of galaxies used in Section 4.1 using the same basis set and format for the plots. The latter quantity is more robust, as can be seen from the reduced bias and scatter in the estimation of t_{10}.

In a similar manner, due to the large amount of stochasticity that realistic SFHs show, it is more robust to estimate the star formation rate (SFR) averaged over the last 100 Myr in lookback time, rather than the instantaneous SFR, as shown in the bottom panels of Figure 12. The panel on the left denotes SFR_{100}, which has less scatter than SFR_{inst}, shown on the right. It is widely appreciated that broadband SED fitting is primarily sensitive to SFRs averaged over the past 100 Myr[8] (Conroy 2013; Johnson et al. 2013), but SED fitting traditionally reports SFR_{inst} in its chosen parametrization nonetheless. With rapid rises and

---

[8] However, when nebular emission lines are strong enough to contribute significantly to the broadband photometry, SED fitting can probe $\sim 10 \, Myr$ timescales.
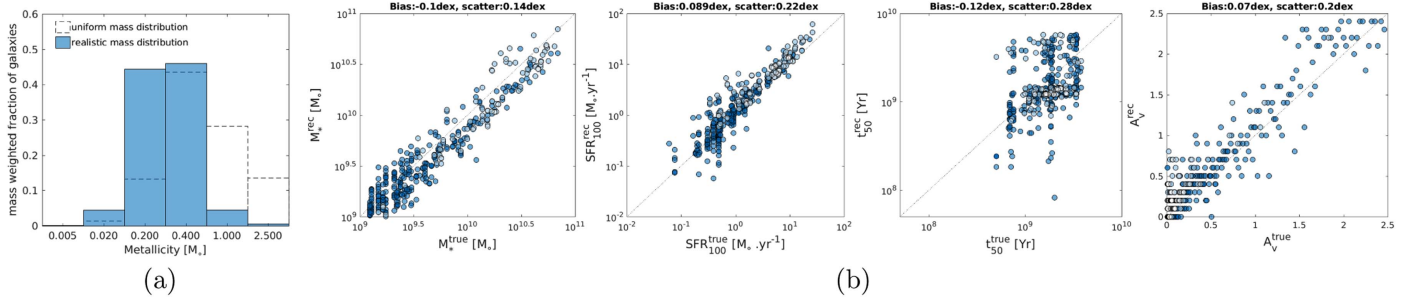
Figure 11. Left: mass-weighted metallicity distribution at present epoch, binned using the BC03 Z range. Solid bars denote the distribution for the sampling in mass used in Section 4.1, while the dashed lines denote the distribution for a uniform sampling in stellar mass. Right: SED fits to the ensemble of SAM galaxies taking the range of realistic metallicity values into account. The t_{50} reconstruction has a reasonable scatter of 0.28 dex that looks poor due to the small distribution of true values. The fits are further complicated by dust, but still comparable to the ones with a single metallicity value.

exponential declines possible, these quantities can differ significantly, leading to the extra scatter in the bottom right panel of Figure 12.

5.2. The Number of Episodes of Star Formation Experienced by $1 < z < 1.5$ CANDELS Galaxies

It is an important feature of the dense basis method to be able to recover the number of strong episodes of star formation in a galaxy. Doing so allows us to detect recent bursts of star formation, or a period of relative quiescence between episodes of continuous star formation, with the amount of data that can be extracted depending upon the S/N. This can then be used to infer valuable information about the galaxy's evolution and merger history.

In this paper, we have demonstrated the use of an F-test to detect if the addition of a second component of star formation is a statistically significant improvement to the fit. This is then used to infer the fraction of galaxies whose SFHs contain a second major episode of star formation, and was validated for the mock galaxies in the high S/N regime in Section 4.1. For our current sample of 1100 CANDELS GOODS-S galaxies, we can reliably fit 790 galaxies, with the remaining galaxies either having poor χ^2 or with missing fluxes in multiple filters, preventing robust estimation of the SFH and its uncertainties. The F-test then determines that 134 galaxies out of the sample of 790 galaxies show a statistical improvement upon being fit with a second component, of which 117 galaxies contain a second episode of star formation. This corresponds to roughly 15% of the sample, similar to the results for the mocks. Figure 13 shows six examples of the procedure, showing three galaxies that were fit by a single basis SFH and three with two components.

Additionally, we provide a breakdown of the fraction of galaxies in each mass bin from $[10^8, 10^{10}]\,M_\odot$ shown in Figure 14. This figure reveals a significant decrease in the fraction of galaxies that are fit with two major episodes of star formation as the stellar mass increases above $10^{9.5}\,M_\odot$. As seen in Section 4.1, we expect to underestimate the fraction of two-episode galaxies at lower masses in the CANDELS sample. Hence the increased number of two-episode galaxies at $M_* < 10^{9.5}\,M_\odot$ is a robust indication that two-episode galaxies are more common at lower mass. This discrepancy between the data and simulations is intriguing.

5.3. Constraints on Timing and Duration of Episodes

Using the reconstructed SFHs for our CANDELS sample, we can obtain constraints on the timing and duration of episodes of star formation. This is possible since the reconstructed SFH using our well-motivated basis SFH set captures the general trend of star formation, even if the finer stochastic details are lost. For each fit, we obtain the number of episodes of star formation, the lookback time of peak star formation, and the FWHM of that episode, thus obtaining the timescale of star formation episodes both on a galaxy-by-galaxy, as well as an ensemble basis, as shown in Figure 15. For $\sim$40% of the galaxies, we find that the SFH is still rising at the time of observation, comparable to $\sim$30% for galaxies from the SAM and hydrodynamic simulations. In estimating the width of an episode of star formation, we estimate the width of an episode up to the time of observation, leading to truncated widths for the subsample of galaxies whose SFHs are still rising, shown in red in the histogram. We find that the widths for our sample are smaller by a factor of $\sim$10 than those for the mock galaxies. This discrepancy bears further investigation, with a similar difference seen in Diemer et al. (2017). Additionally, we can also find the interval between episodes of star formation for the galaxies that are reconstructed with two episodes of star formation.

5.4. Statistics of t_{10}, t_{50}, t_{90} and Uncertainties

The reconstructed SFHs for the CANDELS galaxies computed using the dense basis method are used to compute the lookback times at which the galaxy accumulates a certain fraction of its observed mass. These quantities, defined t_x, satisfy the equality,

$$\int_0^{t_x} \psi_k(t')dt' = \frac{x}{100}\int_0^{t_{obs}} \psi_k(t')dt' \implies M_*(t_x)$$
$$= \frac{x}{100}M_*(t_{obs}). \qquad (20)$$

Generalizing t_{10} from Section 5.1, this lets us follow the mass assembly using the lookback times at which the ensemble of galaxies accumulated a certain fraction of its observed mass. We do this for the CANDELS sample at $1 < z < 1.5$ in Figure 16, providing histograms showing the overall lookback times at which the individual galaxies accumulated 10%, 50%, and 90% of their observed stellar mass. This allows us to infer the overall growth and evolution of galaxies at that epoch.
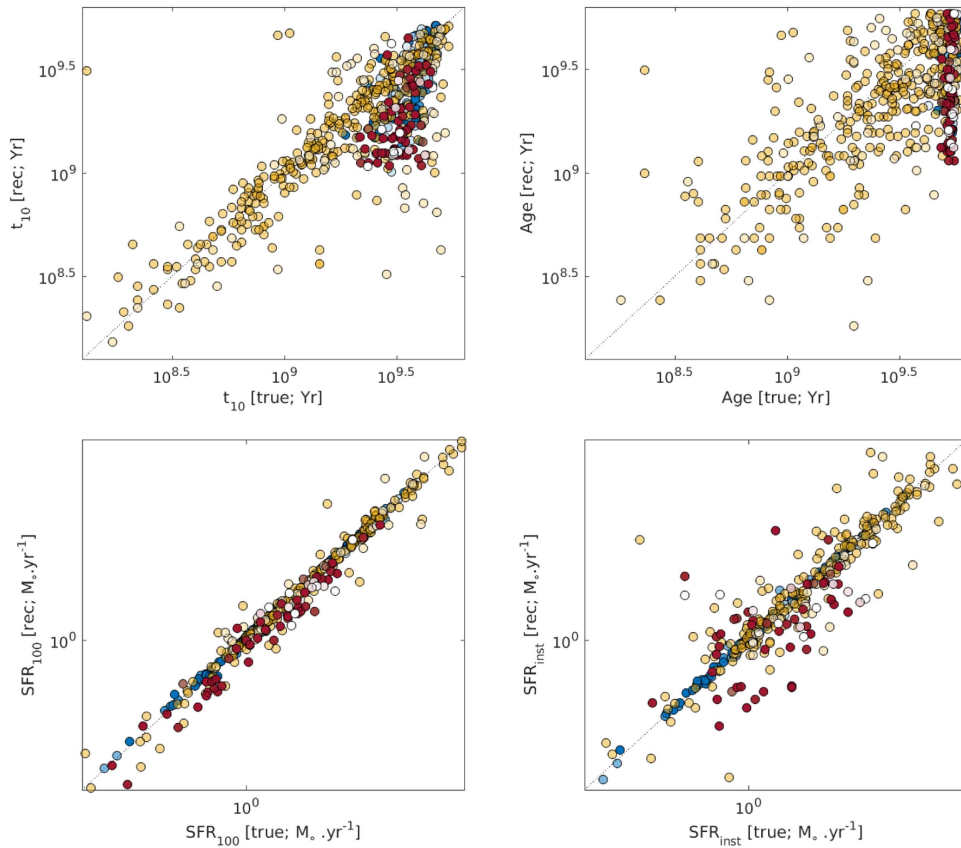
Figure 12. Top: plots showing the ability to extract t_{10}, the lookback time at which the galaxy has accumulated 10% of its observed mass, is much more reliably estimated than the "age ($\equiv t_0$)" of that galaxy with both reduced bias: -0.13 dex for t_{10} vs. -0.19 dex for age, and reduced scatter: 0.24 dex for t_{10} vs. 0.31 dex for Age. Bottom: an illustration of a similar robust measure with SFR_{100} showing less scatter than SFR_{inst}. For the SFR_{100}, the bias is -0.03 dex and the scatter is 0.11 dex. For the SFR_{inst}, the bias is -0.04 dex and the scatter is 0.37 dex. The three different colors show fits to the three different mock data sets, with blue for galaxies from the SAM, yellow for the stochastic galaxies, and red for galaxies from the hydro. simulations, using the same notation as Figure 8.

6. Discussion

6.1. Biases from Using Single SFH Parametrizations

The flexibility in the choice of SFH family used for SED fitting makes it possible to quantify the bias introduced in the estimation of physical quantities due to the choice of SFH parametrization used. We briefly list these biases at $z \sim 1$ for the six families of SFHs presented in this work, highlighting the particular families that perform best at the estimation of a particular quantity. For the seven physical quantities Q_i listed in Tables 3 and 4 below, we formulate the bias and scatter as the median and standard deviation of the histogram $b(Q) = \{1 - Q_i^{rec}/Q_i^{true}\}$, which gives the scatter after taking the bias into account. This is done using physical quantities computed using the reconstructions of the SFHs of the 1200 mock galaxies from Section 4.1 with a realistic mass distribution, using fits without dust or noise to highlight the bias due to the SFH parametrization. We have included the CSF, Top-Hat, and Exponential biases in Table 3 below in an effort to standardize quantities in comparison to older literature, while also listing the reduced bias and scatter with the full dense basis method with up to two components of basis SFHs from the Linexp, Besselexp, Gaussian, and log-normal families. In order to ensure a fair comparison, all families contain the same number of basis SFHs and are dense enough to converge, i.e., a denser grid on the parameter space does not change the results significantly.

Almost all the families tend to underestimate the stellar mass. However, the scatter in M_* is generally larger than this bias except for the Top-Hat family. The scatter is even larger for SFR_{100}, and thus the bias does not significantly affect the results except at the low SFR ($SFR_{100} < 10^{-1} M_\odot$. yr^{-1}) end, as seen from Figure 8. Age has the greatest bias of all the estimated quantities, and it can be seen that it decreases when we estimate t_{10}, which is a more robust quantity, as we proposed in Section 5.1. About 40% of the mock galaxies form $<10\%$ of their mass at $t_{lookback} > 3$ Gyr. The small contribution to the observed flux from these older stars is dominated by more recent contributions, as a result of which the method does detect these older stars and underestimates the age. Since most of the mock galaxies start forming stars at $t \sim t_{bb}$, the distribution of true ages is extremely narrow and can only be underestimated, since the method does not allow $t_{age} > t_{bb}$. An artifact of this bias is also seen in t_{10}, though it is smaller. However, since the dense basis method recovers the major episodes of star formation and the bias is largely due to the distribution of the true ages, the reconstructed SFHs are robust. In a similar vein, the bias decreases in considering t_{50} and even further with t_{90}. Age has a lower scatter than t_{10}, since most galaxies start forming stars at $t_0 \sim t_{bb}$, and this creates a narrow distribution for the true ages. For SED fitting methods that use age, setting Age $= t_{bb}$ would lead to a bias of -23% and a scatter of 32%, fully competitive with any of the single families. The scatter in t_{10} for the dense basis method is also in
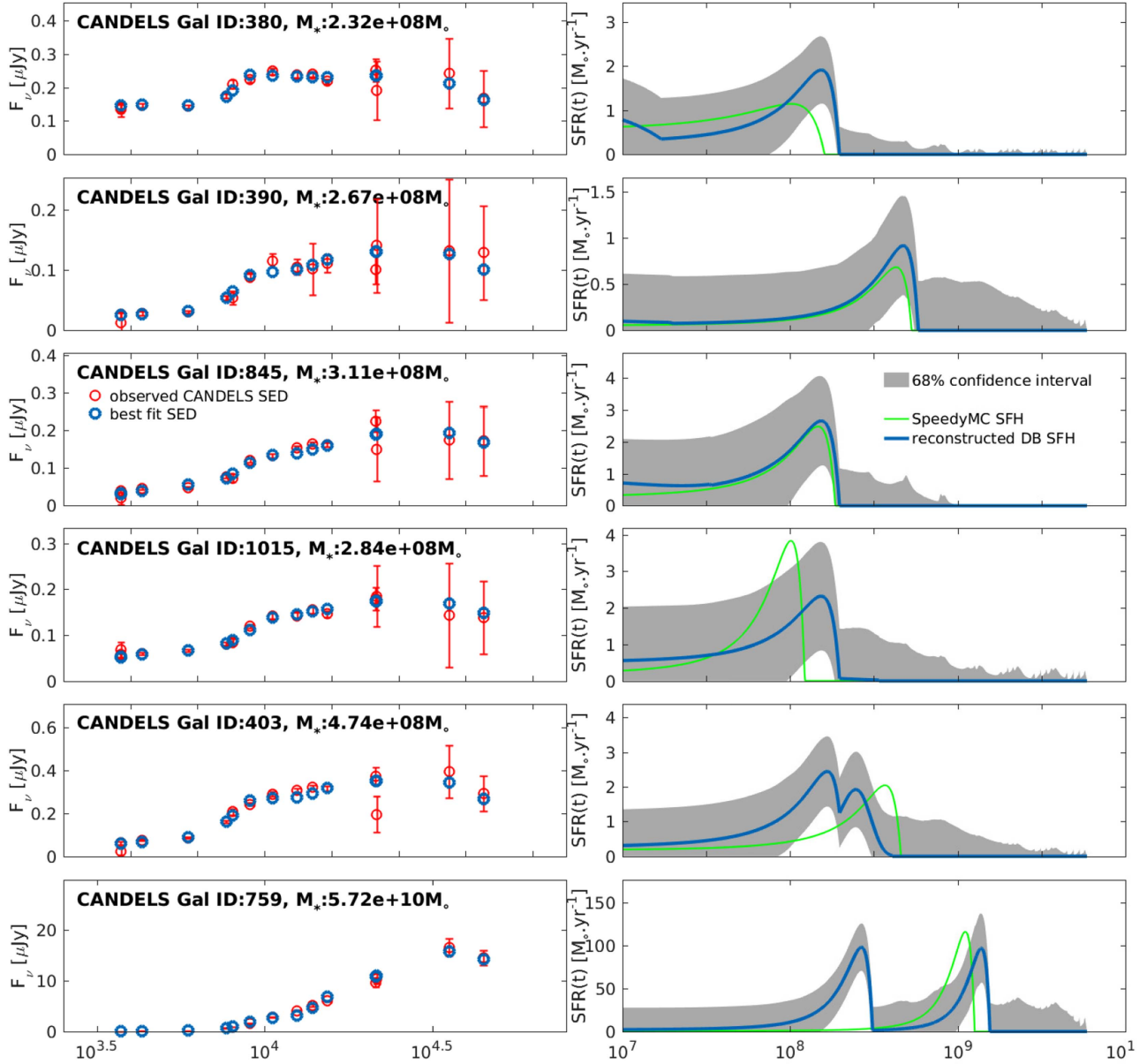
Figure 13. Plots showing a randomly drawn sample from the 790 CANDELS galaxies at $1 < z < 1.5$ used for the validation and results sections of this paper. Left: plots show photometry from CANDELS at $1 < z < 1.5$ (red error bars) and the best-fit SED (blue open circles) using the dense basis method. Right: plots show the single Linexp SFH fit with SpeedyMC in (Kurczynski et al. 2016; green line) and the dense basis reconstruction (blue solid line) with 68% confidence intervals (gray shaded region) computed using the method described in Section 2.5. The χ^2 of the fit for each of the galaxies is 12.7, 7.0, 30.8, 8.7, 40.7, and 41.5, for fits with 15 of the 17 CANDELS bands, excluding IRAC Ch.3,4 since we have not modeled for PAH emission in our atlas. The spectroscopic redshifts of the various galaxies are 1.0910, 1.1300, 1.2510, 1.3810, 1.0760, and 1.2210, respectively.

part due to expanding to a larger parameter space, which yields a smaller bias at the expense of increased scatter regulated by the F-test. The Top-Hat, exponential, and Linexp parametrizations have a large bias in age, and should be accounted for in comparisons of ages in the literature. t_{90} is the most robust of the mass-assembly times, with the Linexp and log-normal families performing best in its estimation. The dense basis method offers the least scatter in M_*, SFR, and t_{90} and is nearly unbiased in these quantities, as well as t_{50}.

6.2. Comparison with Other Methods

The dense basis method offers an SED fitting approach that minimizes the bias and scatter introduced due to traditional SFH parametrizations. In this section, we consider comparisons with existing methods of SFH reconstruction. MOPED (Heavens et al. 2000) fixes logarithmic time bins and finds the SFR in each bin with a piecewise constant SFH using fitting with data compression, giving more weight to those pixels in the spectrum that carry most information about a given parameter. VESPA (Tojeiro et al. 2007) adaptively bins the lookback time, i.e., the t_i in Equation (11), provided there are enough free parameters to avoid overfitting. Dye's (2008) method adopts a similar approach with photometry, but uses regularization in order to the make the SFR in each bin positive, which might bias the likelihood surface and is computationally more expensive. None of these methods reconstructs smooth SFHs; the fits do not provide us with
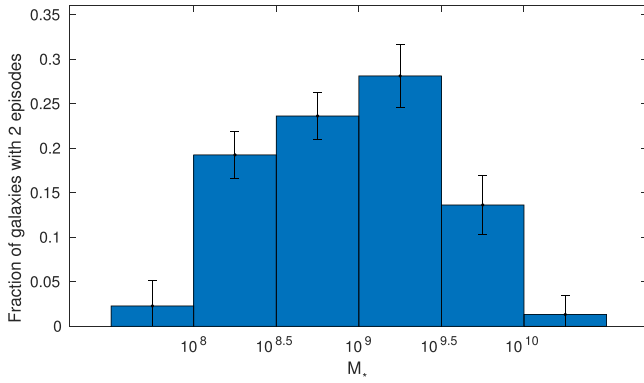
Figure 14. We find the number of galaxies that show a statistical improvement upon being fit with a second component of star formation using the Best4 basis from Section 3.1, and then determine which of those correspond to a second episode of star formation. For the sample of 790 CANDELS GOODS-S galaxies, 15% of the galaxies are fit with multiple episodes of star formation, with the histogram showing the distribution of the fraction of galaxies that are fit with a second episode of star formation across different ranges in stellar mass. The Poisson error bars denote the possible uncertainties due to limited sample size.

SFHs that allow us to analyze the number of episodes of star formation or to analyze the peak times and widths of star formation episodes. The method introduced here uses a physically motivated functional form of SFHs that requires a smaller number of free parameters to fit the SFH, thus obtaining smooth SFHs with multiple components through photometric SED fitting, comparable to what was previously accessible with spectroscopy or CMD reconstruction (Weisz et al. 2011). Another advantage is the ability to use real SEDs to test functional forms for a best match against star formation mechanisms at a given redshift. The usage of well-motivated parametrized functional forms instead of time bins with variable heights allows us to obtain a smooth reconstruction of the SFH with a smaller number of parameters without the need for regularization, since the basis SFHs are smooth and positive definite.

6.3. Possible Extensions of the Dense Basis Method

In addition to the two parameter families described in Section 2.2, it is possible to extend the approach to a larger parameter space by using families of curves including the four-parameter families described in Simha et al. (2014) and the Exponential+ power law (Behroozi et al. 2013),

$$f(t, t_0, \tau, \alpha) = \Theta(t - t_0)((t - t_0)/\tau)^\alpha e^{-(t-t_0)/\tau} \quad (21)$$

where $\tau, \alpha \in \mathbb{R}_+$, and t_0 indexes the time at which star formation begins.

Currently, however, we restrict our attention to the two parameter families since we also consider combinations of curves from these families, which let us model a much more versatile set of trajectories in SFH space.

An advantage of our method is that it will recover only as many SFH basis components as are needed to produce a good fit to the SED, thus enabling us to extend the procedure to reconstructing metallicity histories, and to use multiple dust extinction models. It is also possible to extend the code to additional SPS models, which is naturally incorporated with the Conroy FSPS models (Conroy & Gunn 2010) that contain the BaSTI and Padova isochrone sets. Model dependency due to

the choice of tracks and IMF is also an issue that could be incorporated into future versions, which will have more data available that can be used to address degeneracies between different sets of isochrone synthesis models, stellar evolution tracks, and IMF choices.

Additionally, the superposition of "stochastic" bursts on top of these smooth functional forms has been better shown to reproduce the observed spectroscopic properties of individual galaxies (Kauffmann et al. 2003; Brinchmann et al. 2004). This can be explored in future applications of the dense basis method to spectroscopic data, using realistic stochastic SFHs as in the approach of Pacifici et al. (2015), or the theoretical stochastic SFHs from Kelson (2014).

The current formulation is frequentist, and the training and validation produce parameter uncertainty estimates consistent with this approach. A Bayesian formulation of the method is certainly possible, but since the priors on SFHs are poorly known, significant care would be required.

6.4. Handling Big Data

A large amount of data will be generated from the upcoming generation of surveys including LSST (Ivezic et al. 2008), HETDEX/SHELA (Papovich et al. 2016), and J-PAS (Benitez et al. 2014), which will yield a mixture of broadband photometry and spectroscopy for $N \sim \mathcal{O}(10^8)$ galaxies.

Methods for analyzing these galaxies using SED Fitting techniques need to be both computationally efficient as well as capable of handling and storing large volumes of data in a memory-efficient manner.

The dense basis method was designed with these two requirements in mind. It takes $\mathcal{O}(0.1)s$ for a single run on a 2.9 GHz laptop, albeit with large memory requirements for storing the two-component basis, which runs to $\mathcal{O}(200Gb)$ with 18 values of τ and 99 values of t_0. After the initial generation of the atlas, the fits themselves can be stored simply by saving the index of the best-fit SED and the normalization for each component, leading to efficient storage of the fits as $(N_{\mathrm{component}} * 3)$ coefficients for each reconstructed SFH.

6.5. Broader Data Science Applications

This method can be used to solve problems of the general type

$$\boldsymbol{d} = \sum_i \int_t \boldsymbol{m}_i(t)dt \equiv \sum_i \sum_j a_j \boldsymbol{m}_{ij} \quad (22)$$

where $\boldsymbol{d}$ represents a vector of observables, i.e., galaxy SEDs in the current work, and the functionals m_i represent possible SFHs. The index i sums over basis functions and j refers to multiple photometric bands. We adopt functionals that can be shifted by varying t_0 and scaled by varying τ because this is reasonable for the underlying physics of star formation. This is not a requirement for solving Equation (22) and additional constraints upon the functionals will depend upon the problem being considered. Upon generalization, this formulation is particularly useful for the class of problems where constrained observed data is used to recover quantities in an otherwise inaccessible parameter space, such as single-epoch observations of historical processes. In the absence of a known analytic mapping from the parameter space $\{m_i(t)\}$ to the space of observables $\{d_j\}$ and the lack of a definite correlation between
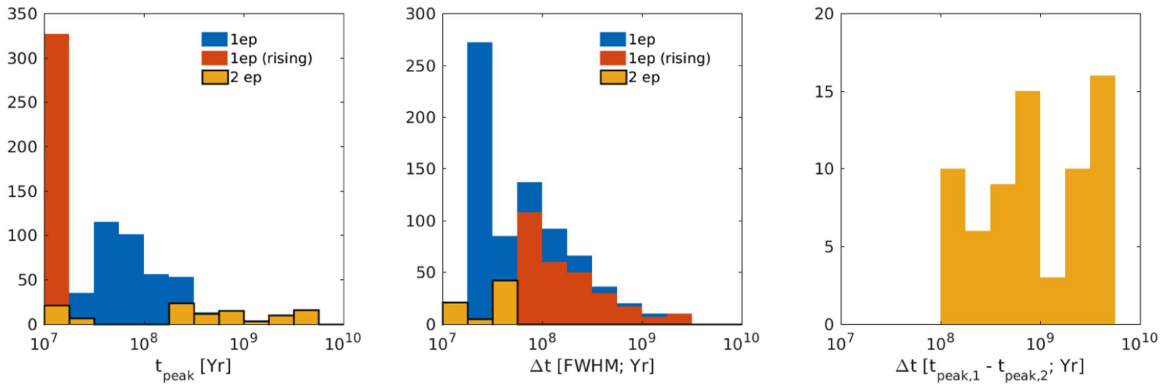
Figure 15. Left: histogram of the lookback time at which the reconstructed SFH for the sample of CANDELS galaxies peaks. The blue histogram denotes the peak times for the galaxies with a single episode of star formation while the smaller yellow histogram shows the peak times whose reconstructed SFH contains two episodes of star formation. A significant fraction of the galaxies have SFHs that are still rising at the epoch of observation, and represent ∼90% of the first bin in the histogram, shown in red. Middle: histogram of the widths of star formation episodes corresponding to the same sample obtained at the FWHM of the reconstructed SFH, with the red histogram representing the portion of the reconstructed SFHs that are still rising, with their widths truncated at the time of observation. Right: histogram of the separation between the two peaks for the SFHs with two episodes of star formation.

the goodness of estimation in these two spaces, traditional methods like Monte-Carlo estimation through the parameter space need not lead to accurate estimation of the m_i, since a good fit need not correspond to an accurate reconstruction of the functional. Methods like principal component analysis may be used in the parameter space, but the principal components do not always correspond to physical representations of the observables. Such situations can frequently arise due to the presence of noise and degeneracies between different parameters that affect the observables.

In such cases, it is possible to apply the training method described in the current work, based on pruning a training atlas from a large space of informed estimates from empirical observations and statistical motivations, leading to an over-sampled non-orthogonal "dense basis." This lets us perform any subsequent fitting to the data in a subset of parameter space where the correspondence between the goodness-of-fit and goodness-of-reconstruction exists and is well defined. Since the functionals in the parameter space are well motivated, they do not span the space of all observables and are robust to noise that would correspond to "unphysical" results. In the current framing, the method is readily applicable to timeseries problems, where the observables are integrated quantities depending on the overall nature of the timeseries.

In an expanding arsenal of data-science tools, the dense basis method provides a convenient formalism to solve the above class of problems in a tractable manner, and to train and implement a solution finding method. The advantages of using this method include not having the constraints of regularization imposed by matrix inversion methods or suffering from the lack of correlation between observables and principal vectors in solution space that techniques like PCA exhibit, while also being robust to noise.

7. Conclusions

The standard assumption of a simple parametric form for galaxy SFHs during SED fitting biases estimations of physical quantities and underestimates their true uncertainties. In this paper, we introduce the dense basis method, which offers a general approach when a vector of observed data points $\boldsymbol{d}$ can be modeled as a sum of positive-definite, continuous functionals $\boldsymbol{m}_i$ obeying $\boldsymbol{d} = \sum_i \int_t \boldsymbol{m}_i(t)\,dt$. Here we apply it to the case where $\boldsymbol{d}$ represents a galaxy SED and the functionals are possible SFHs.

We train the method using SFHs from mock catalogs at $z \sim 1$ from three different sources: a SAM, meshless hydrodynamic simulations, and stochastic realizations. We do this to ensure that the method can successfully reconstruct a wide variety of SFHs, allowing us to relax the assumption that our training SFHs are perfectly representative of the true SFHs of galaxies at that epoch. The training step allows us to compare the goodness-of-fit in SED space to the goodness-of-reconstruction in SFH space. We use this comparison to eliminate SFH families that provide poor or biased reconstructions, leading us to drop the Top-Hat and Exponential families from our basis, while keeping the Linexp, Besselexp, Gaussian, and Lognormal families.

A basis consisting of these four families and their combinations is then used to apply the dense basis method to the broadband CANDELS photometry of a sample of galaxies at $1 < z < 1.5$. The method allows us to accurately estimate physical quantities of interest that explicitly depend on the SFH, notably stellar mass (M_*), and SFR_{100}, which we note is more robust than SFR_{inst} and dust attenuation. The method also allows us to estimate previously inaccessible quantities, including the number and duration of star formation episodes in a galaxy's past, and the lookback times at which the galaxy accumulates 10%, 50%, 90% of its observed mass, which are more robust quantities than the age of a galaxy, and allow us to track the galaxy's growth and evolution as a function of lookback time. The current frequentist implementation of the method allows us to estimate confidence intervals for these quantities. We quantify the bias and scatter in these quantities due to various SFH parametrizations including the traditional parametrizations of constant and exponentially declining SFHs.

The method can be expected to have broad data science applications, and can be scaled and applied to high S/N spectrophotometry from upcoming surveys across all redshift ranges to reconstruct the SFHs of individual galaxies, as well as to infer the growth and evolution of the ensemble of galaxies at various epochs.
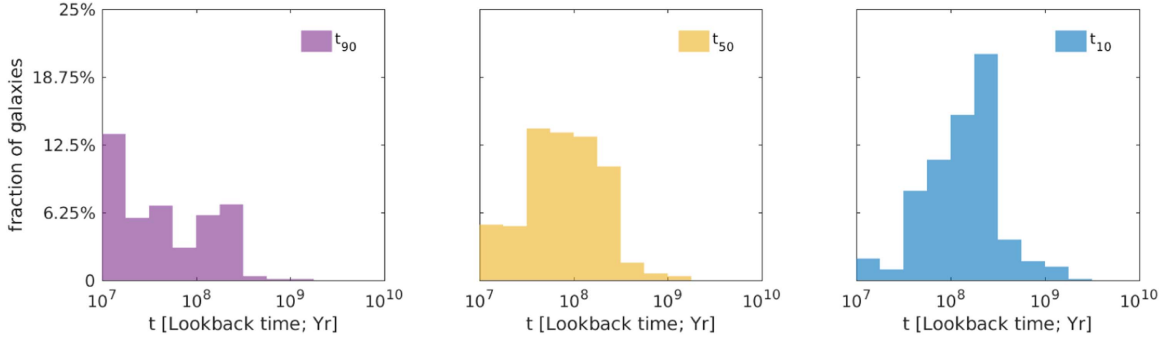
Figure 16. Distributions of the timescales at which the galaxies in the CANDELS sample assembled 90%, 50%, and 10% of their observed mass, showing the fraction of the sample vs. lookback time. The purple histogram shows t_{90}, the yellow histogram shows t_{50}, and the blue histogram shows t_{10}.

Appendix A
Consistency Across Filter Curves

It is possible to perform fits to the mock galaxies observed at different redshifts and ensure that the reconstructed SEDs yield physical quantities that are robust independent of the redshift. This analysis can be extended to determine the redshift range across which a given atlas is robust, since the amount of information contained within the filters changes with redshift.

Since we restrict our mock data set to $z = 1$ and the observed data set to $1 < z < 1.5$ in current work, we perform this consistency check, fitting the same mock galaxies whose rest-frame spectra are computed considering them to be at $z = 1$ and $z = 2$. We perform dense basis fitting on the galaxies, and compare the derived quantities t_{10}, t_{50}, t_{90} and find that the estimation of these quantities remains robust within uncertainties.

Appendix B
Dot-product SED Fitting as a Computational Speedup

We present an additional approach to finding the optimal reconstruction given an atlas of SEDs using a non-orthogonal dot-product, i.e., a projection product, that might prove to be a useful computational speedup for dealing with large data sets.

Since the projection product is done in a non-orthogonal basis, reconstruction of the original vector using the dot-product coefficients is more involved than the procedure in the case of the inner product in an orthogonal space. Various methods have been tested for this reconstruction, including iteratively refitting the residuals as long as they remain above the noise level, constructing a reduced orthogonal space by projecting out components of vectors along a principal component, and constructing an expanded basis of linear combinations of the

basis functionals. This method is expected to operate on the timescale of $\mathcal{O}(N \times M)$ operations, where N is the size of the basis and M is the number of bands of the photometry in consideration.

The best fit is estimated through a non-orthogonal equivalent of a dot-product in the photometric vector space, through a mapping given by

$$\phi(F_{i_1 j}, F_{ij}^{\mathrm{obs}}) = \frac{\sum_j F_{i_1 j} . F_{ij}^{\mathrm{obs}}}{||F_{i_1 j}|| \, ||F_{ij}^{\mathrm{obs}}||} = a_{i_1} \qquad (23)$$

where ϕ is a mapping such that $\phi: \mathbb{R}^{N_{\mathrm{filt}},+} \times \mathbb{R}^{N_{\mathrm{filt}},+} \rightarrow \mathbb{R}[0, 1]$.

For an equivalent orthogonal basis, the dot-product coefficient is given by the same mapping, with an additional constraint imposed due to orthogonality, which is,

$$\phi(F_{i_1 j}, F_{i_2 j}) = 0 \qquad (24)$$

which allows us to reconstruct the original vector simply using

$$F_{ij}^{\mathrm{obs}} = \sum_i^{N_{\mathrm{basis}} \leqslant N_{\mathrm{bands}}} a_i F_{ij}. \qquad (25)$$

However, in the absence of orthogonality, we turn to more involved methods of reconstruction, bounded by both computational costs and error margins on the photometry, which could lead to overfitting if not accounted for.

Other factors held constant, the coefficient of the photometric dot-product indicates the projection of the true SFH of the galaxy onto the basis SFH. Therefore, without any degeneracies in the basis SEDs, a higher coefficient would mean that the SFH is closer to the true SFH of the galaxy, with $a_i = 1$ denoting a perfect match with basis vector i. The procedure returns similar results to the χ^2 fitting procedure described in Section 2.4, with a slight computational speedup requiring $\sim 1/3$rd of the time for fitting an SED, which might be helpful in fitting large data sets of SEDs from upcoming surveys.

Appendix C
Alternative Methods of Defining
Goodness-of-reconstruction

Given that the SFHs are not a directly measurable quantity, care must be taken in comparing the reconstructed SFHs to the true ones, accounting for the unequal sensitivity of the SEDs to the same interval of time at different epochs, as well as the large amount of stochasticity present in the simulated SFHs

Table 3
Bias in the Estimation of Physical Quantities Due to Different SFH Parametrizations at $z \sim 1$. [No Dust or Noise]

	M_*	SFR_{100}	SFR_{inst}	t_{90}	t_{50}	t_{10}	Age
CSF	−14%	5%	4%	−24%	−13%	−19%	−43%
top-hat	−17%	2%	−11%	−27%	−24%	−41%	−59%
exponential	−20%	−2%	−7%	−21%	−34%	−55%	−70%
Linexp	−18%	−1%	−7%	−18%	−28%	−39%	−50%
Gaussian	−16%	−1%	−7%	−20%	−31%	−27%	−16%
log-normal	−14%	2%	−3%	−16%	−25%	−33%	−26%
Besselexp	−19%	−1%	−7%	−21%	−34%	−42%	−43%
Dense Basis	−6%	4%	1%	−4%	−4%	−22%	−29%

Table 4
Scatter in the Estimation of Physical Quantities Due to Different SFH Parametrizations at $z \sim 1$. [No Dust or Noise]

	M_*	SFR_{100}	SFR_{inst}	t_{90}	t_{50}	t_{10}	Age
CSF	28%	43%	40%	36%	48%	51%	37%
top-hat	28%	50%	49%	35%	44%	46%	32%
exponential	27%	16%	20%	34%	36%	36%	26%
Linexp	29%	23%	25%	34%	38%	37%	29%
Gaussian	24%	26%	24%	29%	31%	28%	28%
log-normal	26%	16%	20%	35%	34%	31%	26%
Besselexp	23%	16%	18%	29%	30%	25%	27%
Dense Basis	13%	7%	10%	18%	43%	34%	20%

(SAM, hydro., stochastic). We outline some of the methods viable for this as alternatives to be considered in other applications of the dense basis method. These statistics, while useful for comparing how well a given reconstruction approximates the true SFH, are significantly affected by stochasticity. Since we are only interested in the relative performance of the families of curves in current work, we choose to compare the goodness-of-reconstruction to that of a polynomial fit with the same number of degrees of freedom as the parametrizations under consideration.

1. R^2 *and* R^2 *adjusted:* The coefficient of determination is among the simplest ways to compare two sets of points, comparing how well the reconstructed SFH approximates the true one. This gives the first indication of the fact that some families of SFHs may be more useful than others for a given data set at SFH reconstruction. The R^2 statistic is given by

$$R^2 = 1 - \frac{\sum_t (\psi_{rec}(\log(t)) - \psi_{true}(log(t)))^2}{\sum_t (\psi_{true}(\log(t)) - \langle \psi_{true}(\log(t)) \rangle)^2} \quad (26)$$

which quantifies the amount of variance explained by the fit. Since the stochasticity of the different mocks differs, the median R^2 for fits to the three data sets can vary widely, with the SAM galaxies doing the best and the MUFASA galaxies doing the worst. It is possible to adjust this by smoothing the true SFHs using a nonparametric method until they all exhibit an equal level of stochasticity, or simply by rebinning the SFH with a time interval of the order of the least stochastic sample. Another improvement, as implemented in the current work, is to compare the R^2 of the reconstruction

with a reference R^2 with the same number of degrees of freedom, such as a fit using a polynomial.

2. *The Pearson correlation coefficient:* (ρ_p) Since the standard implementation of R^2 as a goodness-of-reconstruction metric fails to account for the different amounts of stochasticity present in the different mock data sets, we consider the Pearson correlation coefficient, which accounts for the inherent stochasticity of an SFH through a normalization. As an alternative to the previous method, we can present the results for the training step as likelihood versus the Pearson correlation coefficient, written as

$$\rho_{true,rec} = \frac{cov(true, rec)}{\sigma_{true} \sigma_{rec}}$$
$$= \frac{\sum_i (x_i - \bar{x})(y_i - \bar{y})}{\sqrt{\sum_i (x_i - \bar{x})^2} \sqrt{\sum_i (y_i - \bar{y})^2}} \quad (27)$$

since this could better provide an estimate of the goodness-of-reconstruction for highly stochastic SFHs without the need for an additional R^2 adjustment step. However, the coefficient in this form assumes Gaussian statistics, which are not always applicable for our data sets.

3. *Spearman's correlation coefficient:* (ρ_s) Pearson's correlation coefficient assumes a Gaussian distribution of noise around a linear relation, and finds the degree of correlation around it. However, the relation we seek to compare two time-ordered sets of curves, needs to be more robust. Therefore, we considered the Spearman coefficient, which compares two monotonic functions using ranks in order to find the degree of correlation between them. For distinct ranks, the coefficient is given by $r_s = 1 - 6\sum d_i^2 / n(n^2 - 1)$, where d_i is the difference between the two ranks of each observation. This, however does not work very well at describing the fit for young galaxies, where a significant fraction of the two SFHs is tied at the same rank due to long periods of vanishing SFRs at early times.

4. *MISE:* The mean integrated square error given by MISE $= \sum_t \psi_{rec}(\log(t)) - \psi_{true}(\log(t))$ also provides a method to quantify the goodness-of-reconstruction. However, it does have a well-defined range to compare different quantities, and provides no accounting for the varying amounts of stochasticity of the different data sets. The concept of minimum distance estimation that this method implements can also be generalized to the Kolmogorov–Smirnov statistic, which depends on the
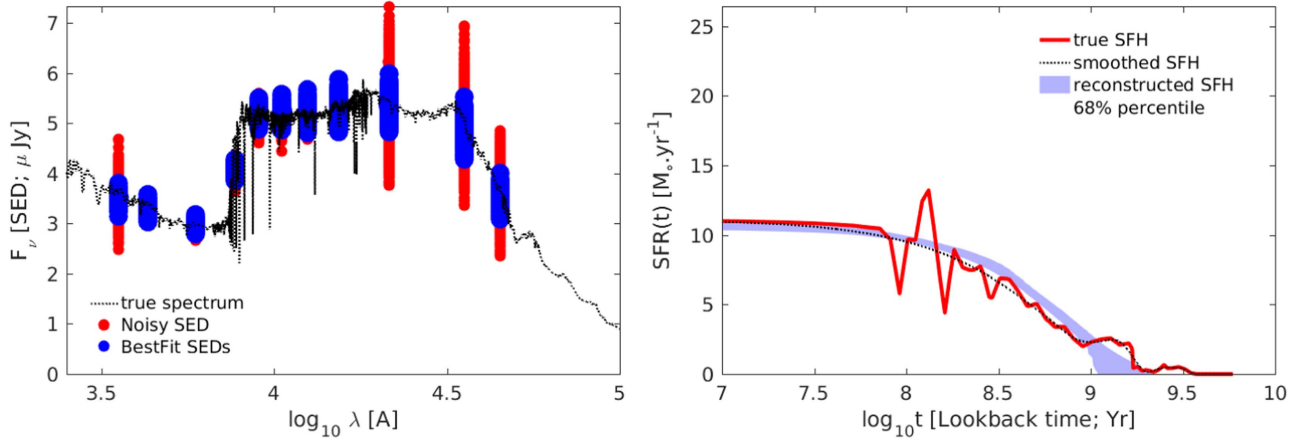
Figure 17. Left: fits using the dense basis method (blue circles) to 1000 noisy realizations (red circles) of the photometry corresponding to a galaxy with true spectrum (black dotted line) showing the robustness of the method to noise that corresponds to unphysical regions of the SFH space. Spectra are shown without nebular emission for clarity. Right: the pointwise 68% intervals of the reconstructed SFHs for each noisy realization (blue shaded region) compared to the true SFH (red solid line) showing that the reconstructions are also largely robust to the noise.
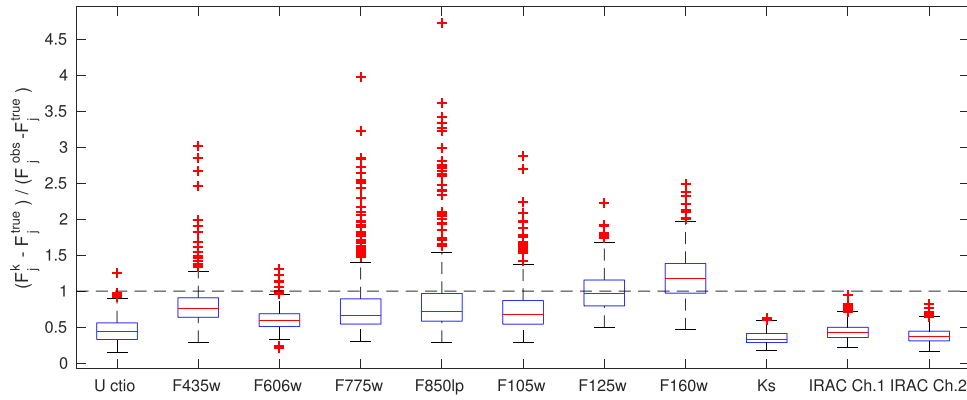

Figure 18. Boxplots showing the results of fitting the ensemble of mocks with multiple noisy realizations and comparing the residuals of the fits to the noise.

maximum absolute difference between the true and estimated cumulative SFHs, but does not provide sufficiently sensitive results to make a distinction between the different families using a correspondence between the statistic and the goodness of fit.

Appendix D
Robustness to Noise

The dense basis method performs SED fitting using an atlas of SEDs corresponding to well-motivated basis SFHs that satisfy the conditions in Section 2.2. Although the mapping from SFH space to the observed photometry is theoretically bijective, an SED at a given noise level for a given set of photometric bands is degenerate in SFH space to the extent that all the SFHs that produce the same SED within error limits are an acceptable fit. Our formulation then ensures that the basis is effectively dense in SFH space, allowing us to reconstruct the overall trend of star formation even if it does not capture the finer stochastic details. However, even though the basis is effectively dense in SFH space, it is not dense in SED space, since a large region of the photometry space is not accessible through any physically motivated SFH. This allows our method to ignore all noise that is "unphysical" while performing the SED-Fitting step. Even though this yields worse χ^2 and the

noise biases the reconstruction to an extent documented in Figure 8, it does not overfit the SED by fitting for any noise that does not correspond to a physically motivated SFH. This allows our method to be robust to a large fraction of the noise, as is seen in Figure 17, where we show an example of 1000 noisy realizations to a SAM spectrum in red and the corresponding reconstruction in blue, which successfully ignores major outliers in fitting the SED. Extended to the entire ensemble of 1200 mock galaxies, we find that the ratio of the residuals to the noise is ∼45%, with a standard deviation of ∼9%, i.e.,

$$\frac{|F_j^k - F_j^{\text{true}}|}{|F_j^{\text{obs}} - F_j^{\text{true}}|} \approx \mathcal{N}(0.45, 0.09). \qquad (28)$$

The decomposition of this quantity into the sensitivity to noise in individual bands in Figure 18 shows that the F160w is the most sensitive to noise, with the method being remarkably robust to the noise in the ground-based bands. The maximum deviation due to noise is computed and found to be in the bounding bands (u ctio and IRAC 4.5 μm). This is expected, since the endpoints are the most unconstrained in the fitting process.

Figure 19. Plot of the correspondence between $\chi^2_{\rm SED}$ and $\chi^2_{\rm SFH}$ for three randomly selected galaxies from each mock data set, using all six families as the basis. The top three rows are galaxies drawn from SAMs (galaxy id = 204, 278, 243), the middle three rows from the hydrodynamical simulations (galaxy id = 270, 5, 228) and the last three rows from stochastic realizations (galaxy id = 74, 109, 60).

Table 5
Comparison of the Goodness of Fit to the Goodness Of Reconstruction for the Ensemble of Mock SFHs

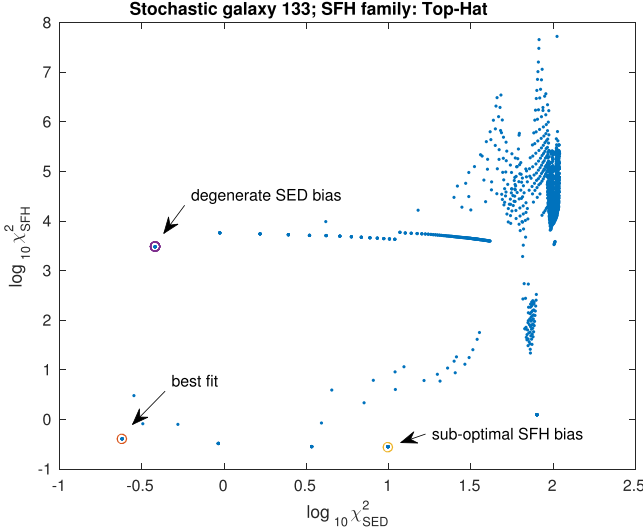|	Linexp	Besselexp	Gaussian	Log-normal	Exponential	Top-Hat
Type 1 bias:	216	179	108	145	323	294
Type 2 bias:	5	2	8	1	10	12

Figure 20. Plot of the correspondence between $\chi^2_{\rm SED}$ and $\chi^2_{\rm SFH}$ for an individual galaxy with the Top-Hat family of SFHs, computed using noiseless fits to the SED. This illustrates the biases that can occur in SFH reconstruction through SED fitting, which we try to minimize through the training procedure.

Appendix E
Examining the $\chi^2_{\rm SED}$–$\chi^2_{\rm SFH}$ Correspondence for Individual Galaxies

We examine the correspondence between $\chi^2_{\rm SED}$ and $\chi^2_{\rm SFH}$ for individual galaxies in greater detail. We provide examples for three randomly chosen galaxies from each mock catalog as examples in Figure 19, and discuss possible biases and how they should be minimized. We compute $\chi^2_{\rm SFH}$ as follows.

$$\chi^2_{\rm SFH} = \int d\left(\log t\right) \frac{\left(\sum_{k=1}^{N_F} \epsilon_k \psi_k(t) - \psi_{\rm true}(t)\right)^2}{\sigma_{\rm SFH}(t)^2}, \qquad (29)$$

where the index k sums over the entire basis of SFHs as above, and ϵ_k denotes the stellar mass normalization. The $\sigma_{\rm SFH}(t)$ denote symmetric pointwise uncertainties computed through the procedure described in Section 2.5 for each family being tested. Since the code is implemented over a grid, the integral over time is effectively a sum over discrete time intervals as described in Section 2.2. The R^2 statistic computes the accuracy of reconstruction and is better for training the basis families, since it does not reward SFH families that yield larger uncertainties, as opposed to $\chi^2_{\rm SFH}$, which does so. However, we can use this statistic to observe the correspondence between fits in SED space and reconstructions in SFH space on a galaxy by galaxy basis, and study sources of biases in the reconstruction.

We encounter two types of biases in the χ^2 plots, summarized as follows.

1. *Degenerate $\chi^2_{\rm SED}$:* If, in addition to the correspondence, some good fits to the SED ($\chi^2_{\rm SED}/{\rm dof} < 1$) correspond to

bad reconstructions of the SFH ($\chi^2_{\rm SFH}/{\rm dof} > 1$), the SFH reconstruction may be biased. However, these are often removed as outliers in the procedure used to compute uncertainties, as described in Section 2.5.

2. *Sub-optimal $\chi^2_{\rm SFH}$:* The best fit to the SED corresponds to a significantly worse reconstruction than the best possible reconstruction of the SFH with that basis. However, like the true SFH, the best possible reconstruction is generally within our reported uncertainties around the best fit determined via $\chi^2_{\rm SED}$.

For the first point, we quantify the two kinds of biases using the χ^2 surface generated for each galaxy in the ensemble of 1200 galaxies using each SFH family. An example of the two kinds of biases is shown in Figure 20, showing the $\chi^2_{\rm SED}$–$\chi^2_{\rm SFH}$ plot for a single galaxy with a single SFH family. Since there is a certain amount of degeneracy introduced in SED fitting due to noise, we consider the set of all good fits ($\chi^2_{\rm SED}/{\rm dof} < 1$) instead of the best fit min($\chi^2_{\rm SED}/{\rm dof}$). As shown in Figure 19, we see that there is generally a good correspondence between $\chi^2_{\rm SED}$ and $\chi^2_{\rm SFH}$ in the regime of good fits. We then find the families that minimize the two types of biases in SFH reconstruction.

We quantify the degenerate $\chi^2_{\rm SED}$ bias by examining the histogram of the set $S = \{\chi^2_{\rm SFH,i} \mid \chi^2_{\rm SED,i} < 1\}$. Since this is the set of good fits, we then say that a galaxy has a type 1 bias if it has multiple peaks in this histogram, separated by a minimum distance of 1 dex in $\chi^2_{\rm SFH}$. This is the more common type of bias, and the probability that it will bias the fit toward a poorer reconstruction depends on the ratio of the areas under the two peaks. We show the number of occurrences of this type of bias for each family in Table 5, finding that the exponential and CSF families have the highest occurrence of this behavior. While these biases are more common than sub-optimal $\chi^2_{\rm SFH}$ biases, they only indicate the possibility of a bias due to noise, and are usually much milder than the example shown.

For sub-optimal $\chi^2_{\rm SFH}$ bias, we find the distance $d = (\chi^2_{\rm SFH}|_{\min(\chi^2_{\rm SED})} - \chi^2_{\rm SFH}|_{\min(\chi^2_{\rm SED})})$ for each galaxy with each SFH family. This distance denotes the difference between the best $\chi^2_{\rm SFH}$ possible in the basis and the $\chi^2_{\rm SFH}$ corresponding to the best-fit SED in the basis. If the latter quantity is much worse than the former, we say that a galaxy has a bias due to sub-optimal $\chi^2_{\rm SFH}$. We find that this is best quantified by the condition $d > 0.4$ dex. We show the number of these biases for each family in Table 5, finding much lower rates of occurrence and that the Top-Hat family shows the highest occurrence of this behavior.

References

Acquaviva, V., Gawiser, E., & Guaita, L. 2011, in IAU Symp. 284, The Spectral Energy Distribution of Galaxies, ed. I. F. Corbett (Cambridge: Cambridge Univ. Press), 42
Acquaviva, V., Raichoor, A., & Gawiser, E. 2015, ApJ, 804, 8
Allen, M. G., Groves, B. A., Dopita, M. A., Sutherland, R. S., & Kewley, L. J. 2008, ApJS, 178, 20

Anderson-Sprecher, R. 1994, The American Statistician, 48, 113
Avni, Y. 1976, ApJ, 210, 642
Behroozi, P. S., Conroy, C., & Wechsler, R. H. 2010, ApJ, 717, 379
Behroozi, P. S., Wechsler, R. H., & Conroy, C. 2013, ApJ, 770, 57
Benitez, N., Dupke, R., Moles, M., et al. 2014, arXiv:1403.5237
Bolzonella, M., Miralles, J.-M., & Pelló, R. 2000, A&A, 363, 476
Bower, R., Benson, A., Malbon, R., et al. 2006, MNRAS, 370, 645
Brinchmann, J., Charlot, S., White, S., et al. 2004, MNRAS, 351, 1151
Bruzual, G., & Charlot, S. 2003, MNRAS, 344, 1000
Calzetti, D. 2001, PASP, 113, 1449
Chevallard, J., & Charlot, S. 2016, arXiv:1603.03037
Cleveland, W. S. 1979, J. Am. Stat. Assoc., 74, 829
Conroy, C. 2013, ARA&A, 51, 393
Conroy, C., & Gunn, J. E. 2010, ApJ, 712, 833
Croton, D. J., Springel, V., White, S. D., et al. 2006, MNRAS, 365, 11
Davé, R., Rafieferantsoa, M. H., Thompson, R. J., & Hopkins, P. F. 2016, arXiv:1610.01626
Diemer, B., Sparre, M., Abramson, L. E., & Torrey, P. 2017, arXiv:1701.02308
Dressler, A., & Abramson, L. 2014, in IAU Symp. 311, Galaxy Masses as Constraints of Formation Models, ed. M. Cappellari & S. Courteau (Cambridge: Cambridge Univ. Press), 140
Dye, S. 2008, MNRAS, 389, 1293
Eisenstein, D. J., Weinberg, D. H., Agol, E., et al. 2011, AJ, 142, 72
Ferreras, I., Rogers, B., & Lahav, O. 2006, arXiv:astro-ph/0611456
Gavazzi, G., Bonfanti, C., Sanvito, G., Boselli, A., & Scodeggio, M. 2002, ApJ, 576, 135
Gladders, M. D., Oemler, A., Dressler, A., et al. 2013, ApJ, 770, 64
Green, J., Schechter, P., Baltay, C., et al. 2012, arXiv:1208.4012
Guo, Y., Ferguson, H. C., Giavalisco, M., et al. 2013, ApJS, 207, 24
Hammer, F., Flores, H., Elbaz, D., et al. 2005, A&A, 430, 115
Heavens, A. F., Jimenez, R., & Lahav, O. 2000, MNRAS, 317, 965
Ivezic, Z., Tyson, J., Abel, B., et al. 2008, arXiv:0805.2366
Johnson, B. D., Weisz, D. R., Dalcanton, J. J., et al. 2013, ApJ, 772, 8
Kauffmann, G., Heckman, T. M., White, S. D., et al. 2003, MNRAS, 341, 33
Kelson, D. D. 2014, arXiv:1406.5191

Kewley, L. J., Dopita, M., Sutherland, R., Heisler, C., & Trevena, J. 2001, ApJ, 556, 121
Klypin, A. A., Trujillo-Gomez, S., & Primack, J. 2011, ApJ, 740, 102
Kurczynski, P., Gawiser, E., Acquaviva, V., et al. 2016, ApJL, 820, L1
Laureijs, R. J., Duvet, L., Sanz, I. E., et al. 2010, Proc. SPIE, 7731, 77311H
Lee, S.-K., Ferguson, H. C., Somerville, R. S., Wiklind, T., & Giavalisco, M. 2010, ApJ, 725, 1644
Leistedt, B., & Hogg, D. W. 2016, arXiv:1612.00847
Leitherer, C., Schaerer, D., Goldader, J. D., et al. 1999, ApJS, 123, 3
Leja, J., Johnson, B. D., Conroy, C., van Dokkum, P. G., & Byler, N. 2016, arXiv:1609.09073
Mandelbrot, B. B., & Van Ness, J. W. 1968, SIAMR, 10, 422
Munshi, F., Governato, F., Brooks, A., et al. 2013, ApJ, 766, 56
Orsi, Á., Padilla, N., Groves, B., et al. 2014, MNRAS, 443, 799
Pacifici, C., da Cunha, E., Charlot, S., et al. 2015, MNRAS, 447, 786
Pacifici, C., Kassin, S. A., Weiner, B., Charlot, S., & Gardner, J. P. 2012, ApJL, 762, L15
Pacifici, C., Oh, S., Oh, K., Lee, J., & Yi, S. K. 2016, arXiv:1604.02460
Papovich, C., Shipley, H., Mehrtens, N., et al. 2016, arXiv:1603.05660
Sanders, R. L., Shapley, A. E., Kriek, M., et al. 2015, ApJ, 799, 138
Simha, V., Weinberg, D. H., Conroy, C., et al. 2014, arXiv:1404.0402
Somerville, R. S., Hopkins, P. F., Cox, T. J., Robertson, B. E., & Hernquist, L. 2008, MNRAS, 391, 481
Somerville, R. S., Popping, G., & Trager, S. C. 2015, MNRAS, 453, 4337
Sparre, M., Hayward, C. C., Springel, V., et al. 2015, MNRAS, 447, 3548
Speagle, J. S., Steinhardt, C. L., Capak, P. L., & Silverman, J. D. 2014, ApJS, 214, 15
Steidel, C. C., Rudie, G. C., Strom, A. L., et al. 2014, ApJ, 795, 165
Tinsley, B. M. 1980, FCPh, 5, 287
Tojeiro, R., Heavens, A. F., Jimenez, R., & Panter, B. 2007, MNRAS, 381, 1252
Tomczak, A. R., Quadri, R. F., Tran, K.-V. H., et al. 2016, ApJ, 817, 118
Weisz, D. R., Dalcanton, J. J., Williams, B. F., et al. 2011, ApJ, 739, 5
Xie, M.-g., & Singh, K. 2013, International Statistical Review, 81, 3
Zhao, G., & Ma, Y. 2016, Statistics Probability Letters, 116, 72